Edge effect: Liquid sheet and droplets formed by drop impact close to an edge

S. Lejeune, T. Gilet, and L. Bourouiba

Phys. Rev. Fluids **3**, 083601 — Published 7 August 2018

DOI: 10.1103/PhysRevFluids.3.083601

Edge-effect: Liquid sheet and droplets formed by drop impact close to an edge

S. Lejeune*
Microfluidics Lab, Department of Aerospace and Mechanical Engineering, University of Liège, Liège, Belgium and The Fluid Dynamics of Disease Transmission Laboratory, Massachusetts Institute of Technology, Cambridge, MA 02139, US

T. Gilet†
Microfluidics Lab, Department of Aerospace and Mechanical Engineering, University of Liège, Liège, Belgium

L. Bourouiba‡
The Fluid Dynamics of Disease Transmission Laboratory, Massachusetts Institute of Technology, Cambridge, MA 02139, US

Asymmetric liquid sheet fragmentation is ubiquitous in nature and potentially shapes critical phenomenon such as rain-induced propagation of foliar diseases. In this experimental study, we investigate the formation and fragmentation of a liquid sheet upon impact of a drop close to the edge of a solid substrate. Both the impact Weber number and the offset, the distance from the impact point to the edge, are systematically varied. Their influence on the kinematics of the liquid sheet and the subsequent statistics of droplet ejection are rationalized. Three major asymmetry scenarios are identified and linked to distinct droplet ejection patterns. Scaling laws are proposed to rationalize these scenarios based on impact parameters.

I. INTRODUCTION

Around 10% of the world crops are still lost due to plant diseases [1] which costs billions of dollars each year [2, 3] and increases pressure on communities [1]. The optimization of timing and amount of sprayed chemicals in the context of smart agriculture requires improved understanding of disease spread in the field [4–7]. Rain was found to be correlated to the dispersal of foliar diseases such as septoria leaf blotch and fusarium head blight, affecting wheat and rice, respectively [8–10]. Prior studies mainly focused on dispersal statistics collected at the level of crop fields or parcels [9, 11–13]. Investigations at the level of leaf and plant remain scarce [11, 14–16]. They are statistical in nature neither accounting for drop-plant interactions nor for the underlying fragmentation physics. Thus, generalizing results to various plants and precipitations remains a challenge [7, 17]. Recent studies have shed new insights on raindrop-leaf interactions [18, 19], identifying the important role of wetting and of sessile drops on leaves. They identified several dispersal mechanisms as a function of leaf mechanical properties that are both common and efficient at dispersing pathogens. One of the main dispersal scenarios on semi-rigid leaves, coined *crescent-moon* (Fig. 1a), consists in the impact of a raindrop in the vicinity of a sessile (contaminated) drop supported by the infected leaf. The sessile drop is stretched into an asymmetric liquid sheet, which then retracts and fragments into a myriad of contaminated droplets ejected away from the plant.

Drop impacts have been studied in many configurations [20–22] including impacts on thin films [23–25], on deep liquid layers [26, 27], or on solid substrates with various wettings, geometries and inclinations [21, 28–32]. Impacts at sufficiently high speed result in a splash, which involves the formation of a liquid sheet, a crown, which then destabilizes into droplets. Previous studies focused on the crown dynamics and droplet ejection in axisymmetric configurations [33–37]. Increasing attention has also been paid to impacts on small solid targets of comparable size to that of the drop diameter [38–42] or binary drop collision [43, 44]. In the *crescent-moon* impact scenario, an intrinsic horizontal asymmetry leads to a non-axisymmetric liquid sheet [19]. This latter induces asymmetry in the speed and direction of ejected droplets. Inclination, compliance and finite size of the leaves all amplify this asymmetry [19]. Drop impacts that yield asymmetric behaviors were also studied: (i) with horizontal gradients of texture and wetting properties [45–50], (ii) with varying inclination or tangential speed of the substrate [51–53], and (iii) with non-axisymmetric target shapes [54, 55]. The relationship between liquid sheet asymmetry and droplet ejections was investigated for a stationary liquid sheet [56]. The mass distribution of ejected droplets has been quantified by [39]. By contrast, the distributions of droplet speed and direction were seldom reported and never fully investigated, though these variables are crucial to assess the dispersal of plant diseases via raindrop impact.

* slejeune@uliege.be
† tristan.gilet@uliege.be
‡ lbouro@mit.edu

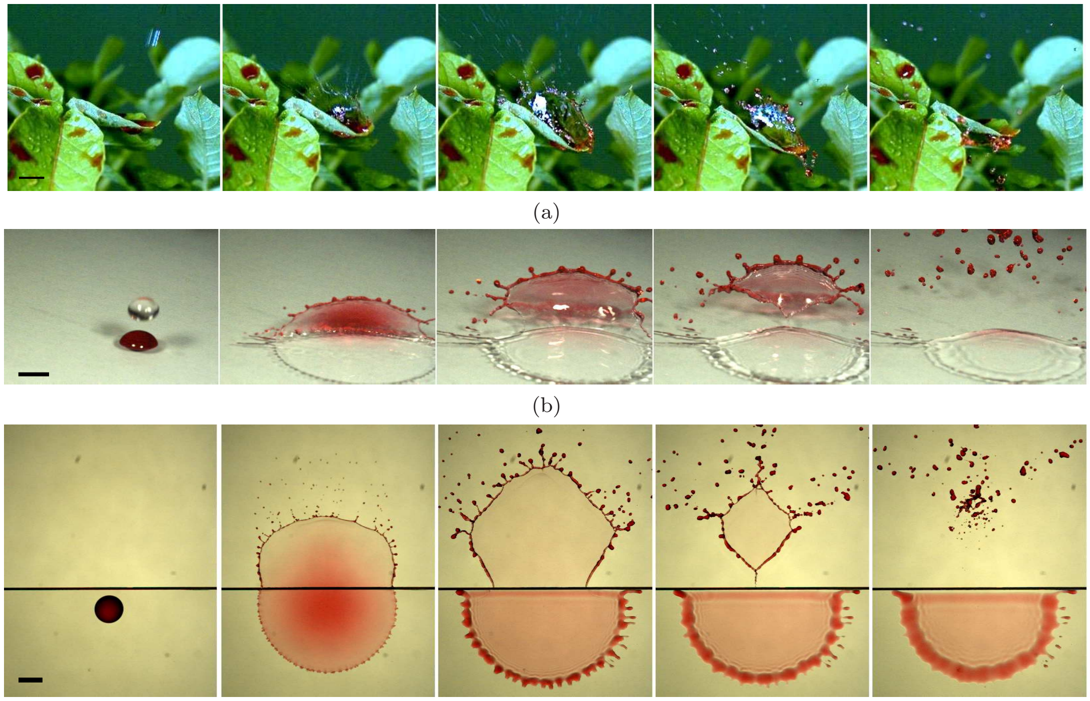

(a)

(b)

(c)

FIG. 1. (Colour online) Liquid sheet formation and fragmentation into droplets, in three configurations. (a) In the field: a raindrop impacts onto a potato leaf on which dyed fluid (red) was deposited. Times are, from left to right, -3, 2, 6, 13 and 29 ms with respect to impact. The sheet is fully three-dimensional. (b) A water drop impacts close to a dyed sessile drop on a flat horizontal dry plexiglass substrate. Times are, from left to right, -1, 3, 8, 11 and 23 ms with respect to impact. The sheet is still fully three-dimensional. (c) Impact of a dyed drop close to the edge of a flat dry plexiglass substrate. Times are, from left to right, 0, 2.5, 8, 10.5 and 14 ms from impact. The sheet remains largely in the plane of the substrate. Scale bars are 5 mm.

Our observation of a large number of drop impacts on wet leaves, in fields and in the laboratory (Figs. 1a and 1b), confirmed the frequent occurrence of asymmetric liquid sheets in the air. These sheets develop either through the *crescent-moon* scenario described in [18], by impacts close to edge of leaves, or by a combination of both. The *crescent-moon* mechanism was reproduced in laboratory conditions with a drop impacting close to a sessile drop on a flat, dry and rigid substrate (Fig. 1b). The key emerging features are: (i) the asymmetric shape of the sheet in the air, (ii) the fluid of this sheet originating mainly from the sessile drop, (iii) a destabilizing free rim at the outer-edge of the sheet, and (iv) the presence of a triple solid-liquid-air contact line. The *crescent-moon* sheet is inherently three-dimensional, hence complex to track accurately.

In this paper, we identify and study one of the simplest impact configurations that produces a sheet with the aforementioned features. It consists in the impact of a single drop close to the straight edge of a flat dry substrate (Fig. 1c). Upon impact, the drop spreads radially until it reaches the edge. It then continues to expand in the air, thereby forming a liquid sheet whose asymmetry varies with the distance from the impact point to the edge. The main goal of this paper is to characterize both the dynamics of this sheet and the number, mass, direction and speed of the ejected droplets, as a function of impact speed and distance of impact point to the edge, referred to as offset. In section II, we present the experimental setup. We then describe the phenomenology of the liquid sheet expansion, retraction and break-up for various impact speeds and offsets in section III. A quantitative analysis of the sheet dynamics and the droplet statistics is presented in sections IV and V, respectively. Finally, results and implications of the asymmetry of the liquid sheet in shaping droplet patterns in the context of rain-induced foliar pathogen dispersal are discussed in the last section.

TABLE I. List of variables and symbols with their definition and typical values

Symbol	Meaning	Value/Range (room T° $\simeq 20°C$)
	Physical properties and initial conditions	
d	offset	2.4 - 12 mm
R_0	initial drop radius	2.4±0.03 mm
V_0	initial drop speed	1.6, 2.3, 3.2, 4.4, 6 ±0.1 m/s
M_0	initial drop mass ($M_0 = 4\pi R_0^3/3$)	57.9 ±2 mg
ρ	water density	1000 kg/m^3
ν	water kinematic viscosity	10^{-6} m^2/s
σ	water surface tension	70±2 mN/m
	Characteristic times and dimensionless numbers	
t_i	impact time - $t_i = 2R_0/V_0$	2.9, 2.1, 1.5, 1.1, 0.8 ms
t_c	capillary time - $t_c = \sqrt{4\rho R_0^3/(3\sigma)}$	16.2 ms
We	Weber number - $We = 2\rho R_0 V_0^2/\sigma$	186 (◯), 367 (▷), 700 (★), 1340 (□), 2435 (◇)
Oh	Ohnesorge number - $Oh = \sqrt{\nu^2\rho/(2R_0\sigma)}$	0.0017
Fr	Froude number - $Fr^2 = V_0^2/(2gR_0)$	50 - 800
	Sheet spreading on solid	
R_s	spreading radius on solid	[mm]
R_{sM}	maximum of R_s	[mm]
t_{sM}	time of R_{sM}	[s]
δ	dimensionless offset - $\delta = d/R_{sM}$	[-]
t_d	time at which the liquid reaches the edge of the substrate	[s]
	Sheet expansion in the air	
l_n	extension of the air sheet normal to the edge	[mm]
l_{nM}	maximum of l_n	[mm]
t_{nM}	time of l_{nM}	[s]
τ_n	dimensionless normal time - $\tau_n = (t - t_d)/(t_{nM} - t_d)$	[-]
l_t	extension of the air sheet tangential to the edge	[mm]
l_{tM}	maximum of l_t	[mm]
t_{tM}	time of l_{tM}	[s]
t_r	time of the sheet collapse along the edge	[s]
τ_r	dimensionless time of collapse along the edge - $\tau_r = (t_r - t_d)/(t_{nM} - t_d)$	[-]
	Droplet ejections	
v	horizontal ejection speed of a droplet	[mm/s]
v_T	average speed of droplets ejected at a given τ_n	[mm/s]
m	mass of a droplet	[mg]
$\Phi(X)$	maximal value of a variable X taken as the cut-off of its CDF	[/]
x	distance travelled horizontally from ejection by a droplet	[mm]
Ψ	asymptotic value travelled by a droplet - $\Psi = \lim_{t\to\infty} x$	[mm]
Ψ_M	maximum value of Ψ	[mm]
$Q_i(X)$	quantile function of a variable X taken at i percent	[/]

II. EXPERIMENTAL SETUP

A syringe pump is filled with dyed water, of surface tension $\sigma \simeq 70$ mN/m, density $\rho \simeq 1000$ kg/m^3 and kinematic viscosity $\nu \simeq 10^{-6}$ m^2/s at room temperature (20 ± 2°C). The syringe is connected to a vertical needle that releases drops of radius $R_0 = 2.4 \pm 0.03$ mm. These drops fall and impact near the edge of a flat horizontal substrate. This substrate is made of dry plexiglass, 2 mm thick, with advancing and receding contact angles for water of 85° and 55° ($70° \pm 15°$), respectively, cut straight with average roughness of 4 μm. The offset d is defined as the distance between the impact point and the straight edge, counted positively when at least half the drop hits the substrate. It is varied in the range $d/R_0 \in [-1, 5]$ with a millimetre stage. Parameters are summarized in table I. The phenomenon is

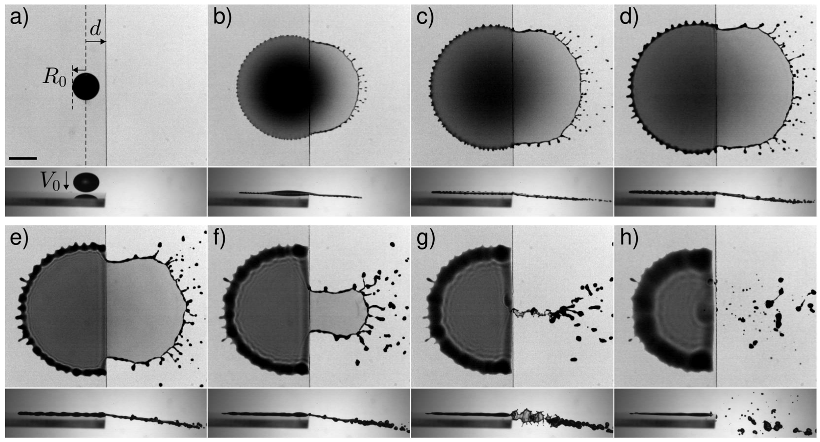

FIG. 2. Drop impact on a flat surface close to its edge, from top and side views. The radius of the impacting drop is $R_0 \simeq 2.4$ mm and the Weber number $We = 1340$. The offset d is defined as the distance between the impact point and the edge. The scale bar is 5 mm and the times are t = 0 ms, 1.6 ms, 3 ms, 4.4 ms, 7 ms, 10.6 ms, 12.4 ms and 19 ms after impact.

recorded from the top with a high speed camera and using backlighting at 2000 frames per second. The inclination of the camera is less than 20° from the vertical, and is accounted for in the image processing. The position and shape of the liquid sheet and the droplets are measured by image processing. Time interpolations of the motion allow for the detection of major events such as the impact of the drop and the entry of the sheet in the air. Five different impact speeds V_0 in the range $1.6 - 6$ m/s were used by changing the height of the needle (table I). The impact speed was determined as a function of the height of release in a different experiment, where the falling drops were filmed from the side. Slight oscillations and flattening of the incoming drop, observed during the free fall right before impact, did not appear to affect the impact dynamics at first order. Local defects that could be present on the edge favored the appearance of nucleation holes that developed from the edge. This generated a notable modification of the sheet dynamics and of its subsequent breakup pattern. This phenomenon is unmistakably identifiable, and we excluded on purpose the very few experiments in which it occurred. Figure 1c shows the process from impact to sheet collapse over 12.5 ms. The impact time of the drops scales as $t_i = 2R_0/V_0 \simeq 1$ ms (table I). The sheet lifetime is closer to the capillary time $t_c = \sqrt{4\rho R_0^3/(3\sigma)} = 16.2$ ms. The Weber number $We = 2\rho R_0 {V_0}^2/\sigma \sim (t_c/t_i)^2$, the ratio of kinetic energy of the impacting drop to its surface energy, is much larger than unity for all our experiments (table I). The Froude number squared $Fr^2 = V_0^2/(2gR_0)$ ranges between 50 and 800, allowing to neglect hydrostatic pressure. Viscous effects can be neglected during impact given that the Ohnesorge number $Oh = \sqrt{\nu^2\rho/(2R_0\sigma)}$ is 0.0017 for the considered size of the impacting drop. In rainfalls, the diameter and terminal speed of raindrops range from 0.5 mm at 2 m/s to 5 mm at 9 m/s, respectively [57, 58]. These parameters yield $We \in [28, 5800]$, $Fr^2 \in [800, 1700]$ and $Oh \in [0.0017, 0.0053]$, fairly close to those considered in our experiments.

III. PHENOMENOLOGY

In Fig. 2, the impact near an edge is presented from synchronized top and side views. Along the edge, the extension of the liquid sheet in the air follows the spread on the solid (Fig. 2b-d). By contrast, the strong retraction of the sheet along the edge is desynchronized from the slight dewetting on top of the substrate (Fig. 2e-g). In the direction normal to the edge, the sheet extends further in the air than it spreads on the solid (Fig. 2b-d). The maximum extension of the sheet is reached first along the edge then normal to the edge (Fig. 2e). The differences in these extension and retraction kinematics normal and tangent to the edge are key in shaping the asymmetric liquid sheet in the air. Droplets are emitted from the corrugated rim at the front of the sheet, as well as from the break-up of the filaments after the collapse of the sheet.

The side view in Fig. 2 shows that the sheet stays approximately in the plane of the substrate throughout the whole process. The droplets are also ejected in this plane, except during the final collapse of the sheet where the antagonistic movements of the rim along the edge give rise to out-of-plane ejections (Fig. 2g-h - side view). The planar and almost horizontal movements of the sheet are crucial for the accuracy of geometric and kinematic measurements from the top view alone. We measured the inclination φ of the sheet from the vertical at its maximal expansion, as a function of offset d (Fig. 3). This inclination first increases linearly with d/R_0 and then reaches a plateau of mean value 87°, independent of We. This value below 90° could be explained by the slight hydrophilicity of the substrate [59, 60]

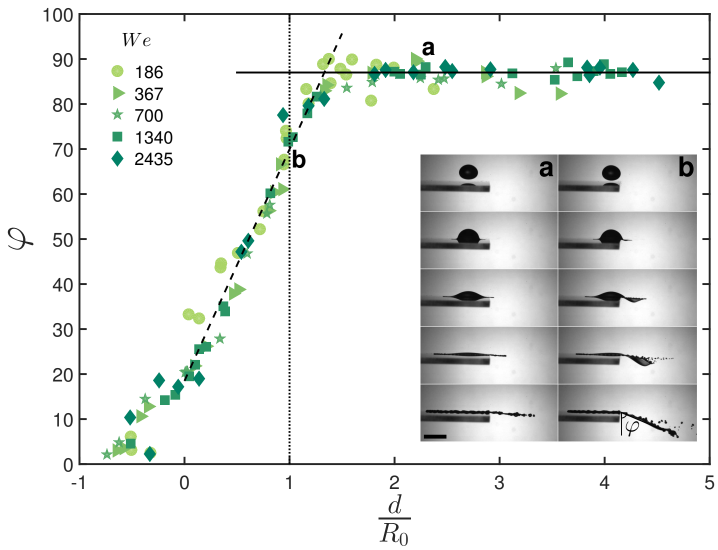

FIG. 3. (Colour online) Inclination φ of the sheet with respect to the vertical as a function of the offset d/R_0 for different We (see table I for symbols of We). The solid line is $\varphi = 87°$ and the dashed line represents Eq. (1). Inset: Side-view time sequence of a drop impacting near an edge at $We = 680$, for $d/R_0 = 2.2$ (a) and $d/R_0 = 1$ (b). Images are taken at -0.2, 0.4, 1, 2.2 and 6.4 ms from the time of impact, respectively from top to bottom. Scale bar is 4 mm.

or by an imperfect transfer of momentum from vertical to horizontal during initial crushing and was also noted for symmetric impacts on poles [42]. A linear fit of the range $d/R_0 \in [0, 1]$ gives

$$\varphi \simeq 53\frac{d}{R_0} + 18. \tag{1}$$

The intersection of this fit with the plateau occurs at $d/R_0 \simeq 1.3$. For larger offsets, the sheet can be assumed to remain in the plane of the substrate (Fig. 3 - inset a). When $d/R_0 < 1.3$ (Fig. 3 - inset b), the deformation of the drop at initial crush brings part of the liquid beyond the edge. This creates a bulge and jeopardizes a planar sheet expansion. The bulge however resorbs during the retraction and the sheet becomes planar again but inclined. In the remainder of this paper, we exclude experiments with $d/R_0 < 1$, for which drops are split by the edge.

Both the shape and the amount of liquid in the sheet vary with the offset. Figure 4 shows four impacts with the same We but different d/R_0. The initial spreading on solid is obviously identical for all, and almost axisymmetric. With a smaller offset, the liquid reaches the edge and enters the air sooner and consequently at higher speed. The extension of the sheet in the air is faster than that on the solid in the perpendicular direction while it follows the extension speed of the solid tangentially to the edge. This anisotropy in extension causes a distortion of the sheet that is more pronounced as the offset decreases. The maximal extensions of the sheet in directions normal and tangential to the edge are reached at different times, which strongly conditions the subsequent retraction. The rim at the front of the sheet becomes more corrugated and emits droplets sooner than the rim close to the edge (Fig. 4b).

As offset is varied, three main scenarios with increasing asymmetry emerge:

(I) When d is sufficiently large (Fig. 4 - row 1), the maximum extension of the sheet is reached simultaneously along and normal to the edge. The shape of the sheet is approximately axisymmetric, analog to spreading on the solid. The sheet retraction is also axisymmetric. Droplets are only emitted during this retraction phase.

(II) As d decreases (Fig. 4 - rows 2 and 3), the maximum extension is both larger and reached later in the direction normal to the edge than tangent to the edge. The retraction of the sheet is mostly dominated by the early motion tangent to the edge. The final shape prior to collapse varies from a small triangle attached to the edge to a rectangle with a width along the edge smaller than its length normal to it. The sheet collapses all at once into a filament (Fig. 4 - rows 2e and 3e-f). The breakup of this filament generates droplets that are significantly smaller than those ejected from the sheet.

(III) Finally at $d/R_0 \sim 1.3$ (Fig. 4 - row 4), the sheet anisotropy is so pronounced that it takes a polygonal shape that is conserved during retraction. The retraction along the edge is completed while it has only started in the

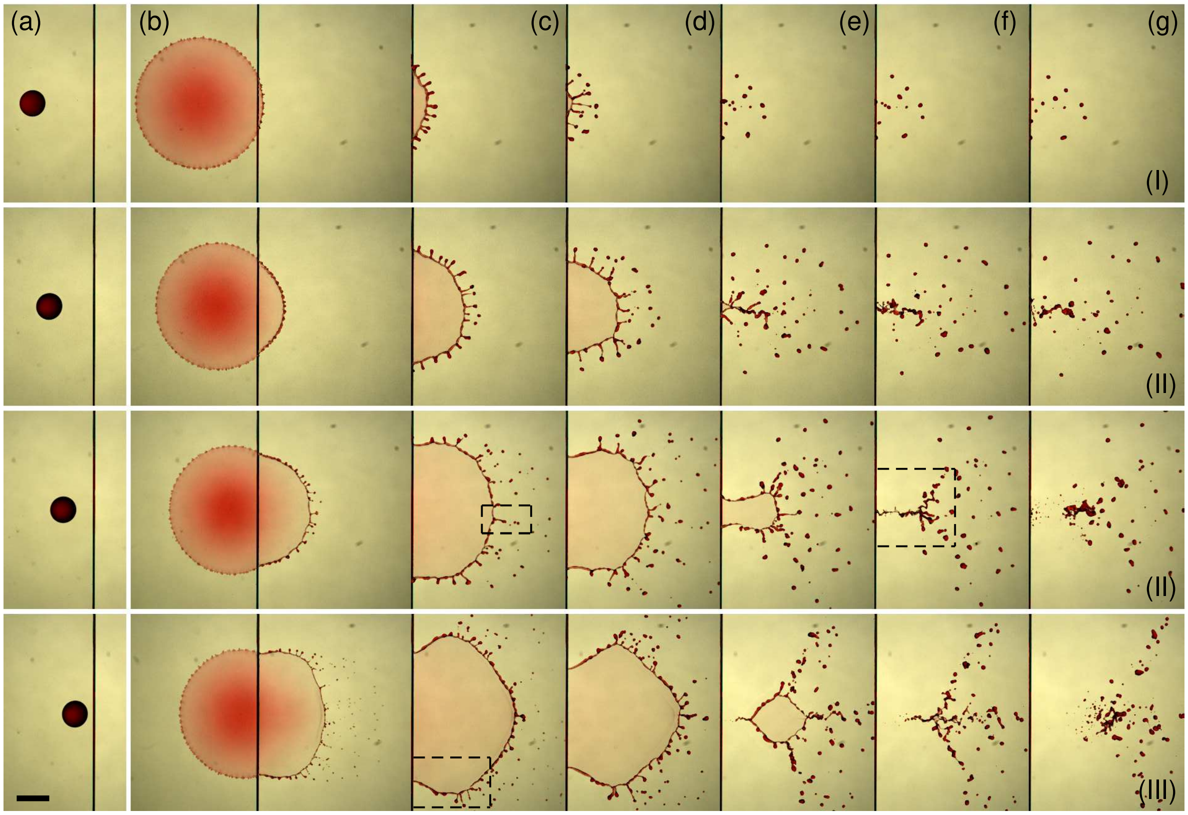

FIG. 4. (Colour online) Time evolution of the sheet in the air for $d/R_0 = 4.4$, 3.2, 2 and 1.3 (top to bottom) and $We = 1340$. Rows 1, 2, 3 and 4 correspond to the retraction scenarios (I), (II), (II) and (III). Snapshots in a same column are taken at the same time t post impact, with $t = 0$ ms, 3 ms, 6 ms, 8 ms, 11 ms, 12 ms, and 14 ms from left to right. Column (a) illustrates the position of the drops right before impact, with respect to the edge. Scale bar is 5 mm. The dashed frames highlight three different droplet ejection mechanisms illustrated in Fig. 16. See Supplemental Material at [61–64] for the videos.

perpendicular direction. The sheet then pinches and separates from the edge before collapse. This pinching also generates a filament that breaks up into tiny droplets.

For a given offset, a variation of the impact speed (and corresponding Weber number) does not strongly modify the shape of the liquid sheet. Three examples of impacts taken at identical $d/R_0 \simeq 1.3$ and different speeds are illustrated in Fig. 5, all leading to scenario (III). Differences are nevertheless observed, both in terms of temporal evolution and size of the sheet. At higher impact speed, the maximal sheet expansion is larger, but collapses sooner. The ejected droplets are also smaller and are ejected sooner.

IV. SHEET DYNAMICS

The scenarios discussed in section III are first summarized in an offset vs. Weber diagram (Fig. 6). For $We \lesssim 186$, only the axisymmetric scenario (I) subsists for $d/R_0 \geq 1.3$.

The sheet kinematics is quantified through the evolution of its extension $l_n(t)$ (resp. $l_t(t)$) in the direction normal to the edge (resp. tangential to the edge), as illustrated in Fig. 7. We also measured the spreading $R_s(t)$ of the liquid on the solid, since this motion is a prerequisite to the expansion of the sheet in the air. These measurements are performed automatically with custom image processing in ImageJ and Matlab. By convention, times are measured from time of impact.

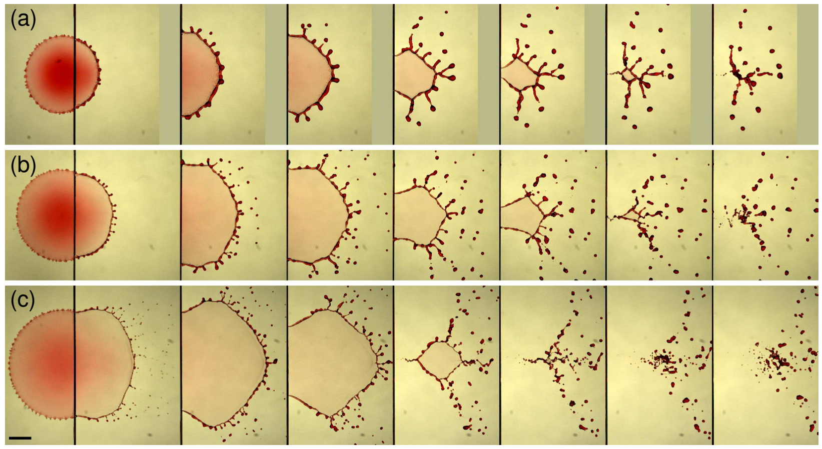

FIG. 5. (Colour online) Time evolution of the sheet in the air for $We = 367$, 700 and 1340 from top to bottom, for $d/R_0 = 1.3$, all leading to scenario (III). Snapshots in a same column are taken at the same time t post impact, with t = 3 ms, 6 ms, 8 ms, 11 ms, 12 ms, 13 ms, and 14 ms from left to right. Scale bar is 5 mm. See Supplemental Material at [64–66] for the videos.

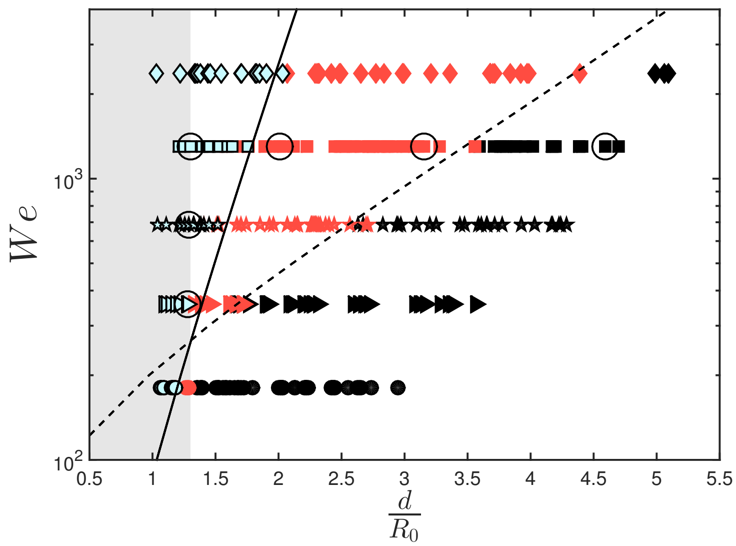

FIG. 6. (Colour online) Phase diagram We vs. d/R_0, in which different sheet asymmetry scenarios are coloured differently: I (black), II (reddish/grey) and III (blue/clear). Symbols correspond to different We, according to table I. The data corresponding to the examples of Figs. 4 and 5 are circled. The shaded region $d/R_0 < 1.3$ corresponds to experiments for which the sheet is not planar. The solid and dashed lines correspond to Eqs. (15) and (16), respectively.

A. Spreading on solid

Upon impact, the spreading radius $R_s(t)$ quickly increases and reaches a maximum R_{sM} in a finite time t_{sM} (Fig. 8a). Slight dewetting is then observed, due to the weak hydrophilicity of the substrate [67]. At first order the expansion dynamics on the solid is not affected by the fact that part of the sheet is then expanding in air. Indeed, the shape of the liquid rim on solid remains circular and centered on the impact point, during the whole expansion and independently of the offset d (Figs. 8a and 8b). During the retraction, we observe capillary waves emitted by the dewetting dynamics, parallel to the edge similar to the ones observed along the rim, on the solid, away from the edge (Fig. 2e-f). They seem to indicate a separation between on-solid and in-the-air dynamics. A travelling wave along the edge following the retraction of the sheet in the air is also visible but its effects appear to be localized close to the edge. Previous analysis of the early time of spreading suggests that the spreading radius $R_s(t)$ increases proportionally to $\sqrt{t}$ [67]. This scaling law can be understood by considering a circle that moves at constant speed towards a straight line. From a purely kinematic point of view, as soon as the circle intercepts the line, the corresponding chord length

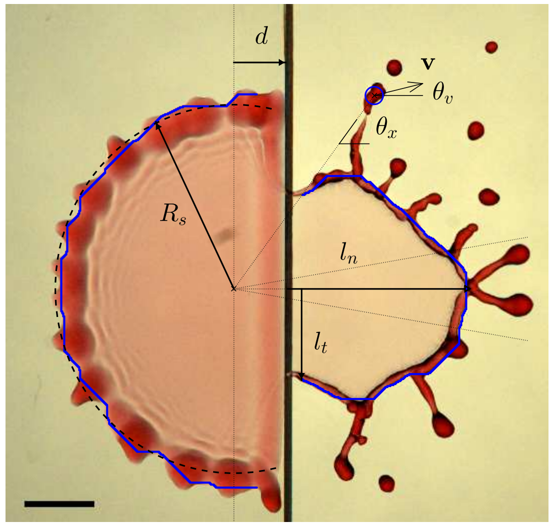

FIG. 7. (Colour online) Main variables that characterize the kinematics of the spreading on solid, liquid sheet in the air, and ejected droplets. The contours (blue lines) are detected by image processing, after thresholding and morphological removal of the corrugations. This particular image is taken 10.5 ms after impact, at offset $d/R_0 = 1.28$ and $We = 367$. Scale bar is 4 mm. The radius R_s of the spreading liquid on solid, the extension of the liquid sheet tangent to the edge l_t and the normal extension of the sheet l_n are represented. This latter is taken to be the quantile 85% in distance to the edge of the contour of the sheet located in a sector of $\pm 10^o$ (fine dotted lines).

grows as the square root of the time from interception. However, at later time the spreading dynamics involves several dissipation mechanisms and there is no simple model that fully describes its kinematics [67–71]. Consequently, we chose to fit an empirical function $R_s(t)$ that grows as $\sqrt{t}$ in the early times and saturates in a finite time:

$$\frac{R_s(t)}{R_{sM}} \simeq \sqrt{\frac{t}{t_{sM}}\left(2 - \frac{t}{t_{sM}}\right)}. \tag{2}$$

Both R_{sM} and t_{sM} are obtained by least square fitting for each individual impact.

The observed maximum spreading R_{sM} increases with We (Fig. 8a - left inset). This variation is well captured by the empirical law of [72]:

$$\frac{R_{sM}}{R_0} = \frac{We^{1/2}}{(1.14 + We^{2/5}\,Oh^{1/5})} \tag{3}$$

where the constant 1.14 is fitted on our data.

The time at which the spreading radius reaches its maximum also increases with We (Fig. 8a - right inset). It can be adjusted with the power-law

$$t_{sM} \sim We^{1/4} t_i, \tag{4}$$

with $t_{sM} = 0.8\,We^{1/4} t_i$ where 0.8 is fitted and $t_i = 2R_0/V_0$ is the impact time (table I). The exponent 1/4 suggests that the time of maximum spreading is almost inversely proportional to $\sqrt{V_0}$, as observed by [30]. The alternative $t_{sM} \simeq 0.3\,We^{3/10}\,Oh^{-1/10}$ proposed by [73] is also in good agreement with our data.

The normalized spreading radius R_s/R_{sM} as a function of the normalized time t/t_{sM} is shown in Fig. 8b. Data from different We collapse onto a single curve, which is very well approximated by Eq. (2) for $t < t_{sM}$. The match between the experimental curves and the equations is not valid beyond $t > t_{sM}$ as dewetting obeys a different dynamics that is sensitive to the surface properties of the substrate. From Eq. (2), we can predict the time t_d at which the liquid arrives at the edge of the substrate ($R_s(t_d) = d$):

$$\frac{t_d}{t_{sM}} = (1 - \sqrt{1 - \delta^2}), \tag{5}$$

where $\delta = d/R_{sM} < 1$ is defined as the dimensionless offset. This equation is also in good agreement with the experimental measurements of the time of formation of the liquid sheet (Fig. 8b - inset).

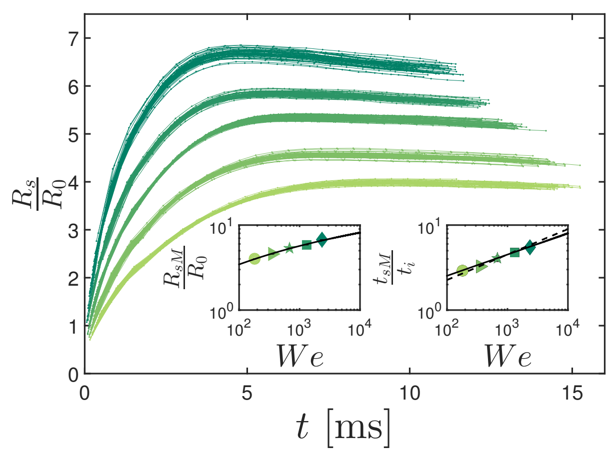

(a)

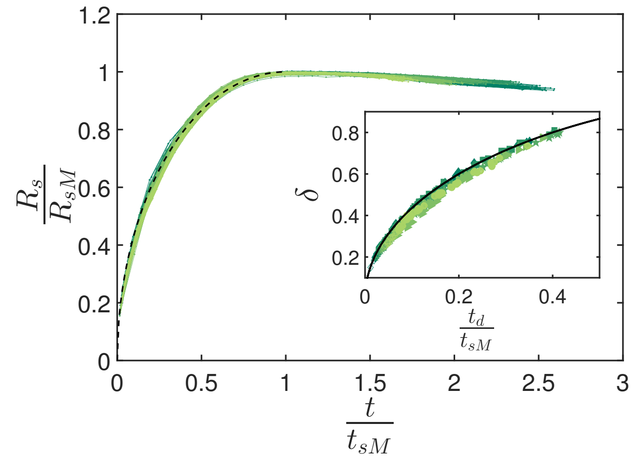

(b)

FIG. 8. (Colour online) (a) Time evolution of the spreading radius R_s/R_0 for increasing We (from bottom to top, $We = 186$, 367, 700, 1340, 2435). Insets: (Left) Maximum spreading R_{sM}/R_0 as a function of We. The solid line corresponds to Eq. (3). (Right) Time t_{sM}/t_i of the maximum spreading as a function of We. The solid line corresponds to Eq. (4). The dotted line is the scaling $t_{sM}/t_i \simeq We^{3/10}Oh^{-1/10}$ from [73]. (b) Rescaled time evolution of the spreading radius R_s/R_{sM} vs. t/t_{sM}, for the five We values in table I. The dotted line shows Eq. (2). Inset shows dimensionless offset $\delta = d/R_{sM}$ as a function of t_d/t_{sM}. The solid line corresponds to Eq. (5). Symbols correspond to different We, all collapsed from 186 to 2435.

B. Expansion/retraction of the liquid sheet in the air, normal to the edge

As soon as it takes off from the edge, the liquid is not subjected anymore to the surface shear dissipation. We describe the extension of the sheet normal to the edge $l_n(t)$ by defining a dimensionless time

$$\tau_n = \frac{t - t_d}{t_{nM} - t_d} \tag{6}$$

from fluid entry in the air $t - t_d$, divided by the time $t_{nM} - t_d$ of maximum extension in the air, normal to the edge. Similarly, the normal extension of the sheet is normalized by its maximal extension l_{nM}. With this normalization, all experimental data collapse onto a single curve

$$\frac{l_n}{l_{nM}} = \tau_n(2 - \tau_n), \tag{7}$$

as shown in Fig. 9a. Interestingly, this shows that the acceleration of the sheet normal to the edge is approximately constant during extension and retraction. The theoretical relations of these results were compared to previous theoretical work on centrosymmetric free sheet. Both the theoretical relations in [38] and [39] for the expansion of axisymmetric liquid sheets, once rescaled, show relative good agreement with our experimental data during the expansion of the sheet, but not during its retraction. The experimental data are better captured by a simple harmonic oscillator in the form $l_n/l_nM = \sin(\pi\tau_n/2)$ as suggested in [74, 75].

Both l_{nM} and t_{nM} are obtained for each experiment by least-square fitting Eq. (7) for each impact. The normal extension is expected to depend both on We and on the history of the liquid on the surface prior to reaching the edge [42]. To investigate this latter dependency, the maximum normal extension l_{nM} is shown as a function of the dimensionless offset δ in Fig. 9b. A linear decrease of l_{nM} with δ is observed,

$$\frac{l_{nM}}{R_0} = 0.36\sqrt{We}(0.9 - \delta) \tag{8}$$

$$\simeq 0.44\frac{V_0 t_c}{R_0}(0.9 - \delta) \tag{9}$$

where the coefficients 0.36 and 0.9 are obtained from best fit and $t_c = \sqrt{4\rho R_0^3/(6\sigma)}$, is the capillary time (table I). The coefficient 0.9 in Eq. (8) indicates that $l_{nM} = 0$ for $\delta = 0.9 < 1$. This is counter-intuitive as it suggests that on the solid, away from the edge, the spreading is slightly larger (by 10%) despite surface shear. However, corrugations

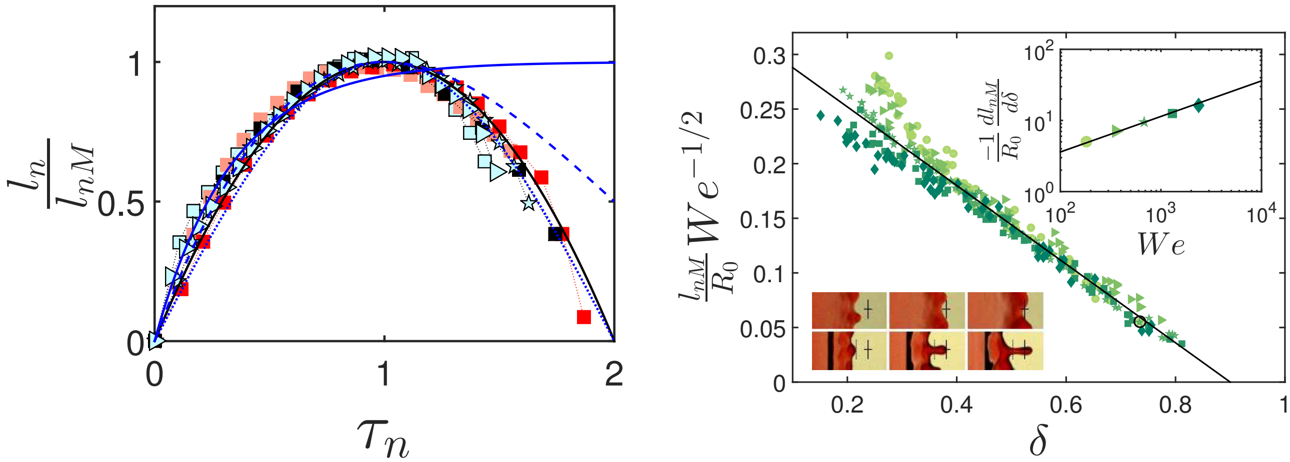

(a)

(b)

FIG. 9. (Colour online) (a) Normalized time evolution of the sheet extension normal to the edge $l_n(t)$ for the six examples of Figs. 4 and 5. The colours represent the different scenarios corresponding to these examples: I (black), II (reddish/grey) and III (blue/clear). The solid black line is Eq. (7). The blue lines correspond respectively to the theoretical results from [38] (solid), from [39] (dashed) and to an harmonic oscillator suggested in [74, 75] (dotted). (b) Maximum normal extension of the liquid sheet l_{nM} normalized by $R_0\,We^{1/2}$ as a function of δ. The solid line shows Eq. (8), which is fitted on all the data points (with $d/R_0 > 1.3$). Symbols for different We are 186 (◯), 367 (▹), 700 (★), 1340 (□), 2435 (◇).

around the sheet form earlier when it is in the air than when it is spreading on the solid. This could be due to the larger deceleration experienced by the sheet in the air than on the solid. Since our measurement of the sheet extension does not include such corrugations: $l_{nM} = 0$ for $\delta = 0.9$.

The acceleration of the sheet in the air normal to the edge is obtained by differentiating Eq. (7) twice: $a_n = -2l_{nM}/(t_{nM} - t_d)^2$. Figure 10a shows that a_n, scaled by $(2R_0)/t_c^2$, is independent of the offset δ. Its average $\overline{a_n}$ over the full range of δ follows a power law in We:

$$\overline{a_n}\frac{t_c^2}{2R_0} = -0.5\,We^{0.6}, \tag{10}$$

where the coefficient 0.5 and the exponent 0.6 are fitted. These dependencies suggest that $\overline{a_n}$ is slightly higher than V_0/t_c.

The time $t_{nM} - t_d$ needed to reach maximum sheet extension is deduced from Eqs. (8) and (10). The ratio gives a dependency in $We^{-0.05}$, negligible at first order. In dimensionless form:

$$\frac{t_{nM} - t_d}{t_c} \simeq 0.6\sqrt{0.9 - \delta}, \tag{11}$$

where 0.6 is fitted. This result matches the experimental data well (Fig. 10b). In summary, the kinematics of the sheet extension normal to the edge as a function of We and δ is well captured by the combination of Eqs. (7), (9) and (11).

C. Comparison to the radial extension in axisymmetric impact configurations

The impact near an edge involves spreading on solid followed by expansion in the air, an intermediate between two axisymmetric configurations already investigated: an impact on infinite solid [72] and a centred impact on a circular target of comparable size to the drop [38] (Fig. 11a). In order to compare the maximum distance reached by the liquid in these three configurations, we performed additional experiments of impacts on a pole. The pole radius d corresponds to the distance the liquid travels on solid before taking off, so it is equivalent to the offset d defined for the impact near an edge. We considered two ratios of pole to drop size, $d/R_0 \in \{1.5, 2.4\}$ and three Weber numbers $We \in \{370, 700, 1340\}$. The substrate material and the impacting drop (size, composition) are the same as for the

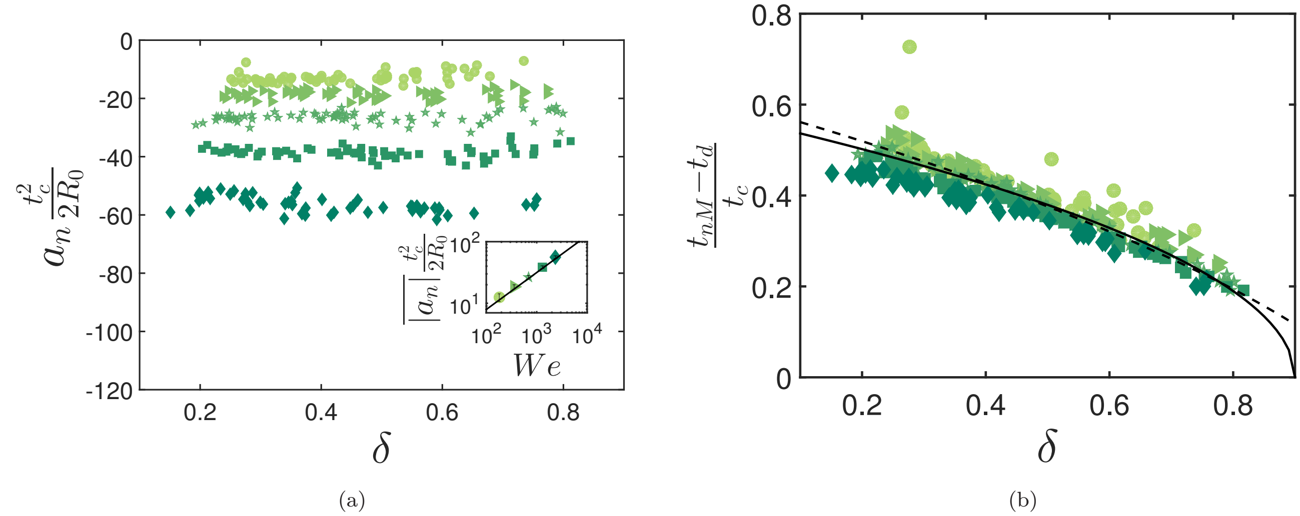

FIG. 10. (Colour online) (a) Non-dimensional acceleration a_n of the sheet normal to the edge as a function of offset δ. Inset shows the absolute value of a_n, averaged over δ, as a function of We. The solid line is Eq. (10). (b) Normalized time of maximum normal extension $(t_{nM} - t_d)/t_c$ as a function of the offset δ. The solid line corresponds to Eq. (11). Symbols in We: 186 (◯), 367 (▷), 700 (★), 1340 (□), 2435 (◇).

edge configuration. Fig. 11b compares prior models of sheet extension: (i) the maximum spreading radius on a solid R_{sM} from [72] [Eq. (3)], (ii) the maximum radial extension of the liquid sheet (from impact point) from [38], and [40]:

$$\frac{l_{nM} + d}{R_0} \simeq \sqrt{We}, \tag{12}$$

with a prefactor 0.22 in Eq. (12) corresponding to the rounded average between the prefactor 0.227 for $d/R_0 \in \{1, 1.4\}$ by [38] and the prefactor 0.22 for $d/R_0 = 1.67$ in [40]. Equation (12) is in good agreement with our experimental data on pole. The power-law $l_{nM} \sim We^{1/2}$ [Eq. (8)] for the edge is similar to the dependence in $\sqrt{We}$ of Eq. (12) obtained for the pole [38, 40].

Fig. 11b shows that the liquid sheet for large We and small offsets goes further than the liquid only spreading on the solid. Indeed, spreading on solid dissipates energy through viscous friction well captured by a Blasius-type boundary layer [42], that reduces liquid spreading. The experimental values of R_{sM} are in good agreement with Eq. (3). More surprisingly, the maximal distance reached by the liquid sheet is always higher with a straight edge than with a circular edge at the same distance d/R_0 from impact point. This is counter-intuitive since in all directions not normal to the straight edge, the liquid spreads more than d on the solid prior to taking-off from the edge. By contrast, in the pole configuration, the liquid sheet forms at the same time after the same spreading distance d in every direction. A possible explanation for this larger distance reached by the sheet from a straight edge is that the rupture of symmetry enables retraction from the back of the sheet leading to further extension normal to the edge.

D. Expansion/retraction of the liquid sheet in the air, along the edge

We proceed by rationalizing the time evolution of the liquid sheet in the vicinity of the edge. As seen in Fig. 2b-d, the extension of the sheet along the edge initially closely follows the spreading on solid during the expansion phase. By contrast, dewetting on solid is much slower than the retraction of the sheet along the edge. This tangential extension should therefore be geometrically related to the spreading law $R_s(t)$ through $l_t(t) = \sqrt{R_s(t)^2 - d^2}$. Combining this equation with Eqs. (2) and (5) yields

$$l_t(t) = R_{sM}\sqrt{1-\delta^2}\sqrt{\tau_s(2-\tau_s)}, \text{ with } \tau_s = \frac{t - t_d}{t_{sM} - t_d}. \tag{13}$$

Again, this square root of time can be interpreted as a kinematic signature of a circle (the sheet) intercepting a straight line (the edge). By identification of Eqs. (2) and (13), we would infer that

$$l_{tM} = R_{sM}\sqrt{1-\delta^2}. \tag{14}$$

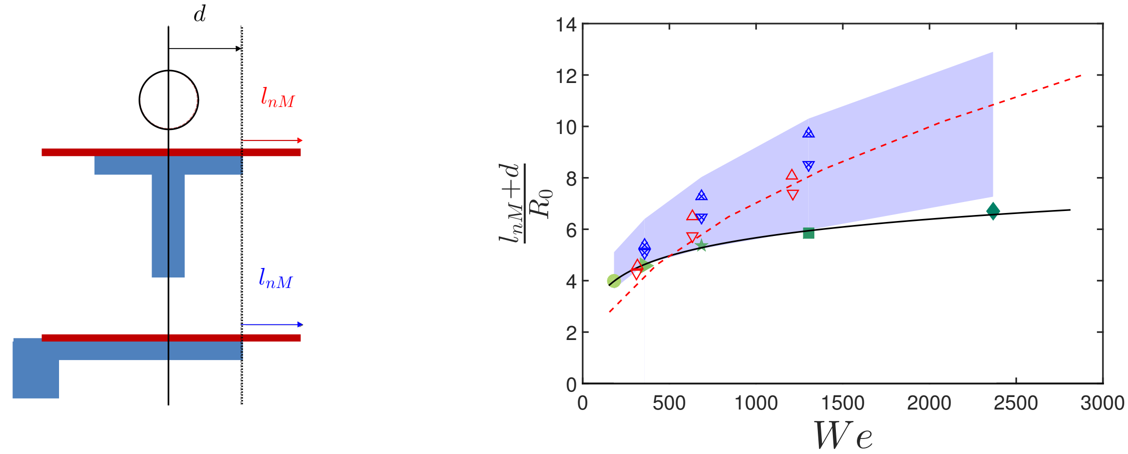

(a) (b)

FIG. 11. (Colour online) (a) Schematics of the geometrical similarity between the sheet extension for the edge and pole configurations. (b) Comparison of the maximum radial distance from the impact point reached by the liquid for three configurations: full spreading on a solid (filled green symbols, R_{sM}/R_0), liquid sheet from a flat edge (shaded area, $(l_{nM}+d)/R_0$), and liquid sheet from a pole (empty triangles, $(l_{nM}+d)/R_0$). Two ratios of pole to drop radius were considered: $d/R_0 = 1.5$ ($\triangle$) and $d/R_0 = 2.4$ ($\triangledown$). The crossed $\triangledown$ and $\triangle$ represent the maximal distance reached in edge experiments with the same offsets d/R_0. The solid and dashed lines correspond to Eqs. (3) and (12), respectively.

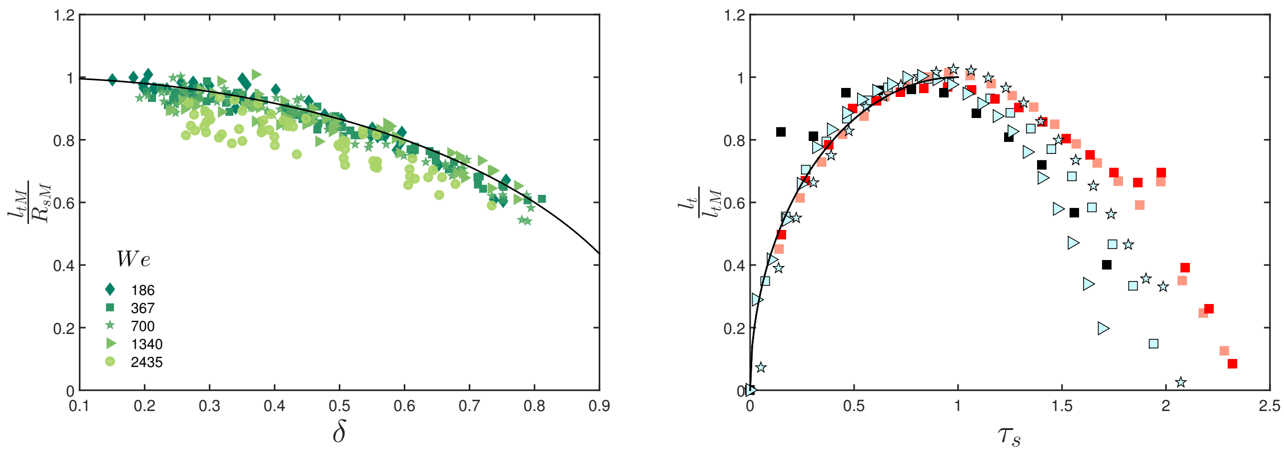

(a) (b)

FIG. 12. (Colour online) (a) Maximum tangential extension l_{tM} of the liquid sheet along the edge normalized by the maximum spreading on solid R_{sM}, as a function of offset δ. The solid line is $\sqrt{1-\delta^2}$, in agreement with Eq. (14). (b) Time evolution of the sheet extension along the edge $l_t(t)$, normalized by its maximum value l_{tM} for the six examples of Figs. 4 and 5. Colours correspond to scenarios: I (black), II (reddish/grey) and III (blue/clear). The solid line for $\tau_s < 1$ represents Eq. (13). Symbols are We: 186 ($\bigcirc$), 367 ($\triangleright$), 700 ($\bigstar$), 1340 ($\square$), 2435 ($\diamondsuit$).

This prediction is fairly well verified by the experimental measurements of the maximum tangential extension in Fig. 12a.

In Fig. 12b, the extension $l_t(t)$ tangent to the edge is represented for the 6 examples of Figs. 4 and 5, normalized by its maximum value l_{tM} and plotted as a function of τ_s. Thanks to this normalization, data from these different experiments collapse well onto the curve of Eq. (13) during the expansion phase ($\tau_s < 1$). However, data from different offsets δ diverge from each other during the retraction phase ($\tau_s > 1$). This scattering of the retraction kinematics along the edge may be linked to the uncontrolled dewetting on this flat vertical edge.

Finally, the time at which the sheet collapses along the edge is defined as $t_r - t_d$. This time is different from the

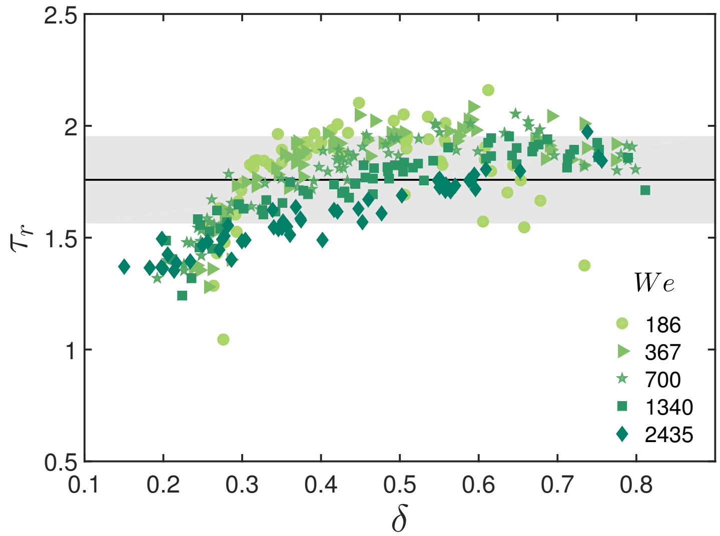

FIG. 13. (Colour online) Normalized time of collapse $\tau_r = (t_r - t_d)/(t_{nM} - t_d)$ of the liquid sheet along the edge as a function of the offset δ. Symbols corresponds to We in table I. The solid line is the average across We and δ and the grey area corresponds to one standard deviation.

full collapse of the liquid sheet only for the experiments of scenario (III). This collapse time normalized by the time of maximum normal extension is defined as $\tau_r = (t_r - t_d)/(t_{nM} - t_d)$ and is illustrated in Fig. 13. It increases from $\tau_r \simeq 1.3$ at low δ, then saturates at $\tau_r \simeq 2$ at large δ. It is only slightly dependent to We for intermediate δ. Its average value is $\tau_r = 1.76$, with a standard deviation of 0.2.

E. Asymmetry and sheet envelope

In Fig. 4, we have observed three qualitatively different scenarios of sheet expansion and retraction. Each scenario is observed in a given region of the diagram ($We, d/R_0$) in Fig. 6. Boundaries between these regions are non-trivial in this diagram. The preceding investigation of the sheet kinematics highlighted the importance of the dimensionless offset $\delta = d/R_{sM}$. Moreover, a key difference between the scenarios is the relative asymmetry of the sheet, which could be represented by the ratio l_{nM}/l_{tM}. The separation of scenarios appears more clearly in the diagram $(\delta, l_{nM}/l_{tM})$ of Fig. 14. With this representation, the transition from scenarios (III) to (II) occurs approximately at

$$\delta = 0.3, \tag{15}$$

and the transition from scenarios (I) to (II) at

$$\frac{l_{nM}}{l_{tM}} = 0.85. \tag{16}$$

The distance travelled by the liquid spreading on the solid strongly influences the subsequent shape of the liquid sheet in the air. Based on this observation, we propose a first-order model to reconstruct the maximal region accessible to the expanding sheet. On the solid, the liquid spreads radially from the impact point and reaches the edge after a distance $d_\theta = d/\cos\theta$, where θ is the angular position from the impact point, measured from the symmetry axis (Figs. 7 and 15). Since d_θ is bounded by R_{sM}, θ must be smaller than $\theta_M = \cos^{-1}\delta$. By replacing d by d_θ (or equivalently δ by $\delta/\cos\theta$) in Eq. (8), we obtain a prediction of the maximum extension l_θ reached by the sheet in direction θ from the normal to the edge:

$$\frac{l_\theta}{R_0} = 0.36\sqrt{We}\left(0.9 - \frac{\delta}{\cos\theta}\right). \tag{17}$$

Since the time of maximum extension varies with the direction considered (i.e., $t_{nM} \neq t_{sM}$), Eq. (17) does not predict the shape of the sheet at a given instant. It rather gives the envelope accessible to the sheet during its expansion,

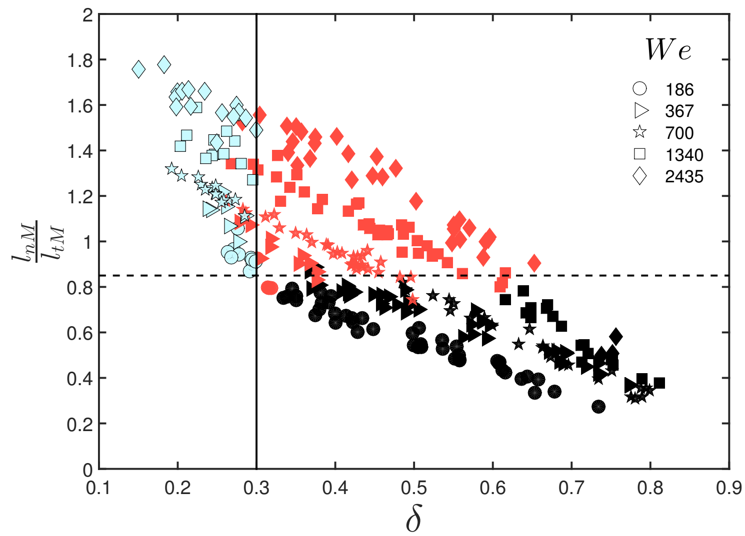

FIG. 14. (Colour online) Scenarios of liquid sheet expansion/retraction, in a $(\delta, l_{nM}/l_{tM})$ diagram. The symbols correspond to different We given in table I and the colours to different scenarios: I (black), II (reddish/grey) and III (blue/clear). The solid and dashed lines correspond to Eqs. (15) and (16) respectively. Horizontal line: $l_{nM}/l_{tM} = 0.85$, vertical line: $\delta = 0.3$.

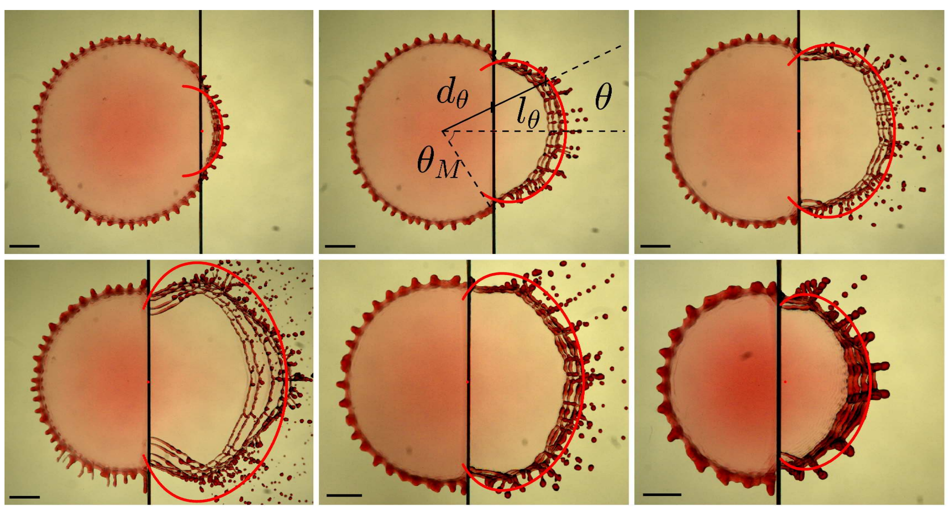

FIG. 15. (Colour online) Time superposition of snapshots from a given experiment, with $t \in [t_{tM}, t_{nM}]$. The curved solid lines (red in online version) represent the reconstructed envelope region accessible to the sheet, predicted by Eq. (17). (Top line) From left to right, $We = 1340$ and $\delta = 0.79, 0.54, 0.34$. (Bottom line) From left to right, $We = 1340$, 700, 367 and $d/R_0 = 1.3$, with $\delta = 0.22, 0.24, 0.28$. Scale bars are 4 mm.

as shown in Fig. 15 for various We and δ. Eq. (17) captures well the sheet outer envelope and only overestimates that envelope for the largest We and smallest d (bottom left picture in Fig. 15) that corresponds to scenario (III). In that particular case, the time of the maximum normal distance to the edge occurs much later than the tangential one which depends on the details of pinning and contact line not captured by Eq. (17).

V. DROPLET EJECTION

In this section, we characterize the ejected droplets from a statistical point of view, and we relate their properties to the asymmetric kinematics of the sheet. We first discuss the mechanisms and direction of ejection then, the initial speed and mass to rationalize the travelled distance of ejected droplets. Finally we take a look at the number of

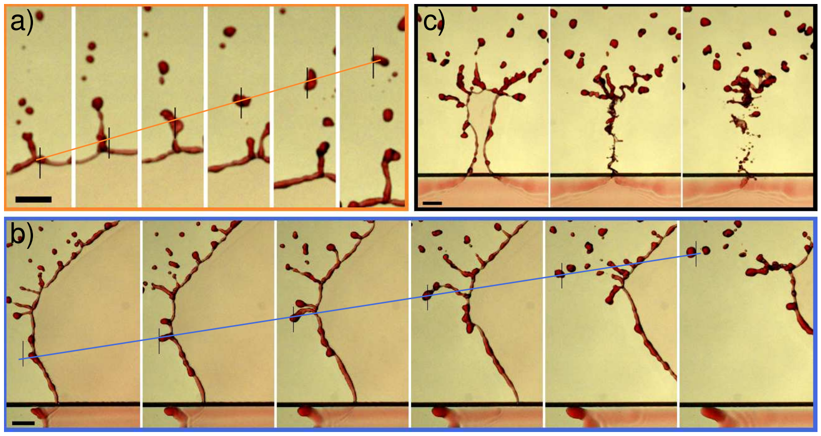

FIG. 16. (Colour online) Mechanisms of droplet ejection: (a) Radial ejection from the rim. Successive snapshots are separated by 0.4 ms, from 6.2 ms after impact. The highlighted droplet is ejected at $\tau_n = 1.02$, with a mass $m = 0.23$ mg and a speed $v = 0.28V_0$. Its ejection angles are $\theta_x = 4^\circ$ and $\theta_v = -9^\circ$. (b) Tangential ejection from the rim. Successive snapshots are separated by 0.6 ms, from 4 ms after impact. The highlighted droplet is ejected at $\tau_n = 1.17$, with a mass m= 0.29 mg and a speed $v = 0.46\ V_0$. Its ejection angles are $\theta_x = 48^\circ$ and $\theta_v = 7^\circ$. (c) Collapse of the sheet. Snapshots are taken at 11.8 ms, 12.2 ms and 13 ms after impact. Scale bars are 2 mm. The orange and blue solid lines join the centre of mass of the ejected droplets across frames. The vertical black lines are at fixed position, so they highlight the left-to-right motion of the droplets. These three snapshots correspond to zooms on the droplet ejections framed in Fig. 4. Panels b) and c) display also a small part of the solid substrate. The edge is then the horizontal black line.

ejected droplets and we summarize the effect of sheet asymmetry on droplet distributions. More details on droplet tracking and mass estimation are provided in appendix A.

A. Ejection mechanisms and direction of ejection

Three ejection mechanisms are identified and illustrated in Fig. 16. They are differentiated according to the time, position, and directionality of the ejections (Fig. 17). The selected snapshots correspond to parts of the movies illustrated in Fig. 4.

- The first mechanism is called radial ejection (Fig. 16 - a). It concerns droplets from the rim of the sheet (i.e., before sheet collapse), for which the ejection direction θ_v is closely aligned on the radial position from the impact point θ_x (definition in Fig. 7). Each droplet originates from a corrugation along the rim. This corrugation grows in a radial filament (almost normal to the sheet) by inertia, owing to the constant deceleration of the sheet. The filament then destabilizes into one or several droplets that are ejected perpendicularly to the rim. The droplets mostly inherit the normal velocity that the sheet had during the early growth of the corrugations. They also inherit a small velocity tangent to the rim, that corresponds to a slight lateral displacement of the corrugation.

- The second mechanism is called tangential ejection (Fig. 16 - b) and it again concerns droplets ejected from the rim of the sheet. In this case, the ejection direction θ_v is not aligned anymore on the radial position θ_x. This mechanism mostly appears on the sides of the sheet in the most asymmetric scenarios, i.e., (II) and (III). Owing to inertia, the corrugations in which liquid accumulates travel along the rim, away from the edge. When the rim retracts tangentially to the edge, these corrugations destabilize into droplets. However, the velocity inherited by the droplets now mostly comes from the motion of the corrugations along the rim, and not anymore from the velocity of the sheet. Consequently, these droplets are ejected in a direction almost parallel to the rim, and perpendicular to its retraction velocity. As the capillary force from the sheet does not directly oppose the motion of these corrugations, the resulting droplets tend to go faster than the droplets ejected radially. This is illustrated in Fig. 16.

- The last mechanism occurs when the sheet collapses (Fig. 16 - c). The resulting liquid filament has a very complex shape and it breaks up in a wide variety of droplets. These droplets may inherit from the late retraction speed of the sheet. A particular collapse event is present when the sheet retracts in scenarios (II) and (III). The two rims of the sheet near the edge converge quickly towards each other. Their violent collision generates many

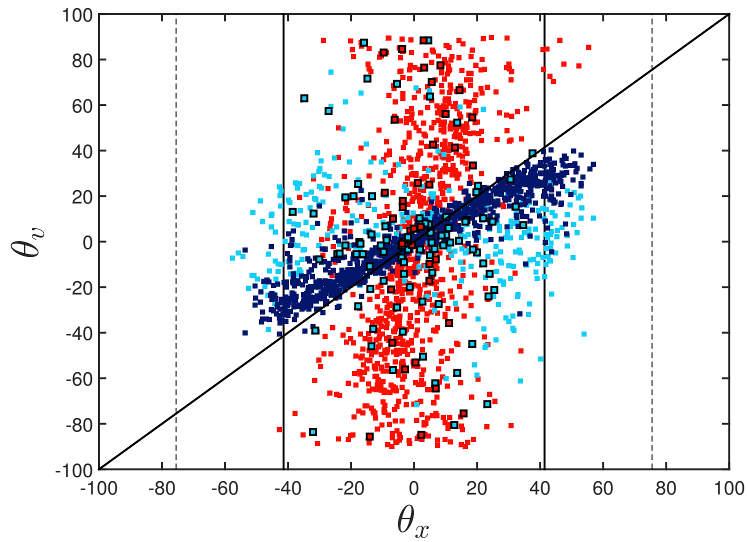

FIG. 17. (Colour online) Angle of the ejection velocity θ_v as a function of the angular position of ejection θ_x measured from the impact point (defined in Fig. 7), for $We = 1340$. Symbols without black contour (resp. with black contour) correspond to $\delta \in [0.2, 0.3]$ (resp. $\delta \in [0.7, 0.8]$). The colour refers to the ejection time: (dark blue) during sheet expansion, i.e., $\tau_n < 1$, (light blue) during sheet retraction, i.e., $1 < \tau_n < \tau_r$, and (red) after sheet collapse, i.e., $\tau_n > \tau_r$. The inclined solid line is the bisector $\theta_v = \theta_x$. The vertical lines correspond to the maximum sheet angle θ_M (defined in Fig. 15), for $\delta = 0.25$ (dotted) and $\delta = 0.75$ (solid).

droplets that are much smaller than those emitted from the first two mechanisms. The direction of ejection can also be out of the plane of the sheet (Fig. 2g-h).

The prevalence of each ejection mechanism is observed in Fig. 17, where the direction θ_v of droplet ejections is plotted against their angular position θ_x. Droplets are distinguished according to the sheet kinematics (expansion, retraction, collapse) at the moment of their ejection. During sheet expansion ($\tau_n < 1$), most droplets are ejected radially, i.e., with $\theta_v \simeq \theta_x$. Tangential ejections only appear during sheet retraction ($1 < \tau_n < \tau_r$), when the sheet asymmetry is sufficiently developed. At small offset δ, most of them satisfy $|\theta_v| < |\theta_x|$, so their ejection direction is more normal to the edge than a droplet ejected radially from the same position. Droplets ejected from the collapse of the sheet ($\tau_n > \tau_r$) remain localized close to the symmetry axis, in $|\theta_x| \lesssim 20°$. However, their ejection direction θ_v is much more scattered than for other mechanisms.

The radial ejection mechanism was already observed in the axisymmetric configuration of impact on a pole [38, 39], and the mass distribution was characterized. The collapse mechanism is also observed in such impacts when the sheet experiences local piercing [38, 39] - this typically occurs when the impact is not perfectly centred on the pole. The tangential ejection mechanism and the filament breakup are not present in axisymmetric impacts such as impact on pole.

B. Droplet ejection speed

We now examine how the mechanisms of ejection can affect the speed of the droplets through the asymmetry of the sheet. The speed v at which each droplet is ejected is represented as a function of its ejection time in Fig. 18a, for the six examples of Figs. 4 and 5. The speed v is naturally normalized by the impact speed V_0, while the time τ_n is normalized by the time of maximum extension of the sheet normal to the edge. All the data corresponding to normal extension ($\tau_n < 1$) collapse onto a single curve, so v/V_0 is a decreasing function of τ_n only, for all We and δ. The ejection speed becomes more scattered as soon as $\tau_n > 1$, i.e., during the retraction and collapse of the sheet. The time τ_r at which the sheet collapses along the edge also corresponds to a maximum scatter of the ejection speed.

The influence of the sheet kinematics on droplet ejection can be better assessed by looking at the speed of the sheet in the direction normal to the edge [derived from Eq. (7)]:

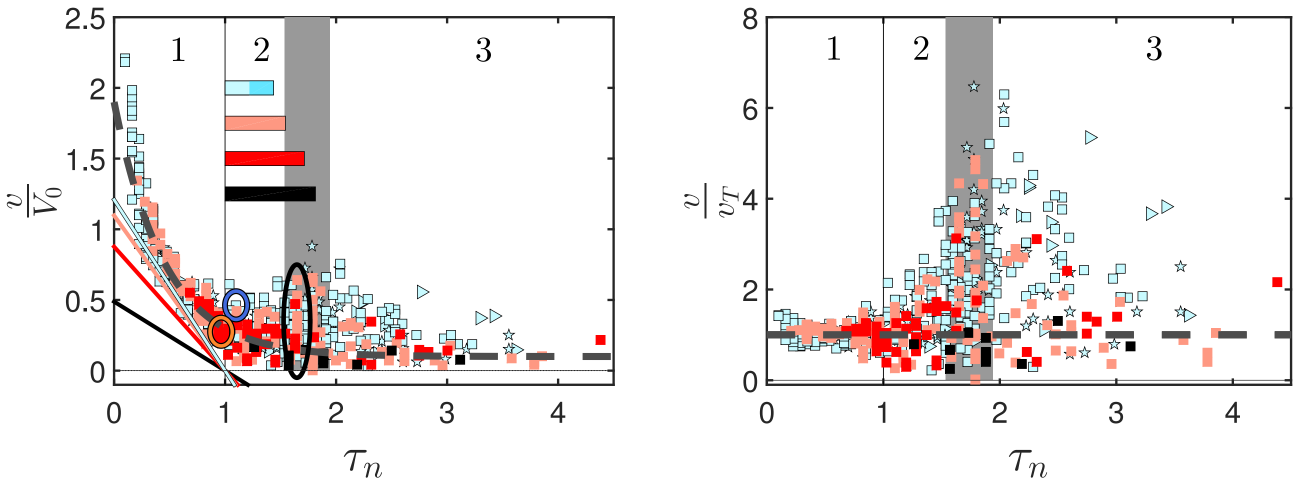

(a)

(b)

FIG. 18. (Colour online) Time evolution of the droplet ejection speed v (a) Normalized by the impact speed V_0 (b) Normalized by v_T, for the six examples of Figs. 4 and 5. The time τ_n is normalized according to the normal extension of the sheet. Each data point corresponds to a single droplet. Symbols correspond to Weber number, We = 367 (▷), 700 (★), 1340 (□), while colours indicate degree of asymmetry from lowest (I) to highest (III) with I (black), II (reddish/grey) and III (blue/clear). The grey area indicates the time τ_r at which the sheet has fully retracted from the edge (average across We and δ, plus/minus standard deviation). The numbers 1, 2 and 3 indicate periods of time of the sheet (1 - sheet expansion, 2 - sheet retraction and 3 - after full sheet retraction along the edge). In (a), horizontal rectangles represent the duration of the sheet retraction. The darker blue rectangle in scenario (III) corresponds to the retraction of the sheet after it has pinched from the edge. The inclined solid lines correspond to Eq. (18) for the six examples (one line per scenario). The dotted line represents Eq. (19). Circled data points correspond to the snapshots of Fig. 16.

$$\frac{1}{V_0}\frac{dl_n}{dt} = \frac{2l_{nM}}{V_0(t_{nM}-t_d)}(1-\tau_n) \simeq 1.47\sqrt{0.9-\delta}(1-\tau_n). \tag{18}$$

The normal extension speed of the sheet is again proportional to the impact speed V_0 at first order. It is reported in Fig. 18a, where it sets a lower limit to the droplet ejection speed. Indeed, ejected droplets during the sheet expansion must go faster than the sheet from which they detach.

A careful examination of Fig. 18a indicates that, for $\tau_n > 1$, the scattering of ejection speed at a given time depends on the considered scenario. In order to better quantify this scattering, we define the average speed $v_T(\tau_n)$ of all the droplets radially ejected at a given τ_n. These considered droplets are from all scenarios together when $\tau_n < 1$, and only from scenario (I) when $\tau_n > 1$. This average velocity is well approximated by:

$$\frac{v_T}{V_0} = 2.1e^{-2.5\tau_n} + 0.1, \tag{19}$$

as illustrated in Fig. 18a. The deviations of the ejection speed from v_T are visible in Fig. 18b.

Data from scenario (I) align in the continuity of the curve observed for $\tau_n < 1$, without much scattering. The corresponding droplets are radially ejected, through the same mechanism as all the droplets ejected in $\tau_n < 1$. By contrast, the ejection speed at $\tau_n > 1$ is much more scattered for scenarios (II) and (III), which suggests the emergence of tangential ejections. The filament breakup occurs in τ_r and it coincides with the maximum of scattering for these scenarios.

The scattering of ejection speeds can be investigated more systematically through the definition of averages over specific time intervals for all experiments at given (We, δ). These averages are defined for any variable X as follows:

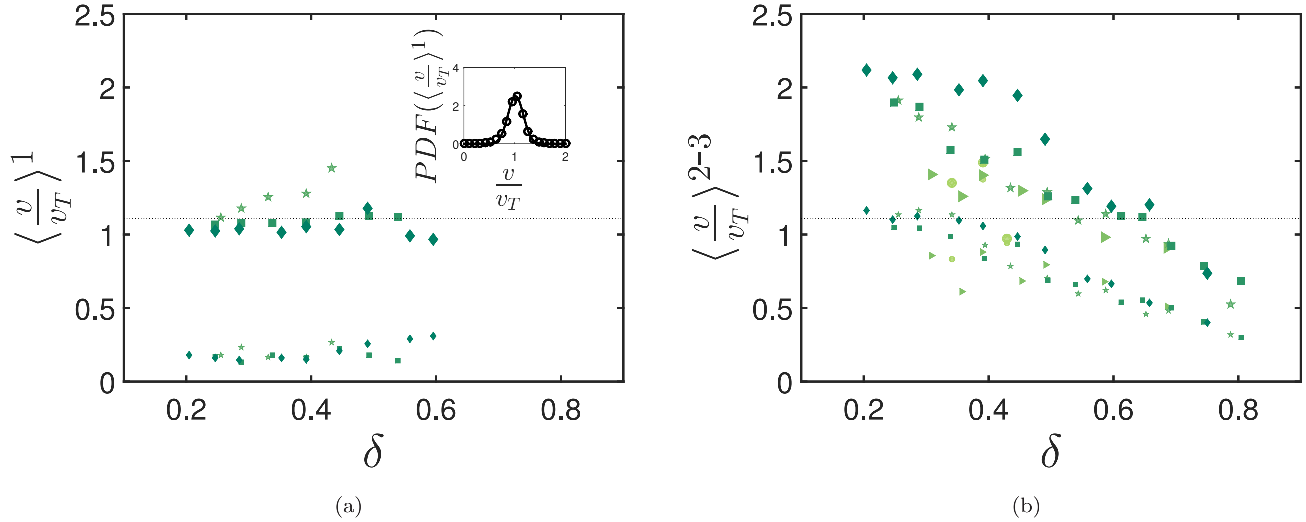

FIG. 19. (Colour online) Average (large symbols) and standard deviation (small symbols) of v/v_T for each (We, δ). (a) Over the sheet expansion ($\tau_n < 1$). The dotted line is the average over all (We, δ). Inset: PDF of v/v_T during the sheet expansion. The solid line is a fit with a Gaussian distribution of mean 1.05 and standard deviation 0.2. (b) After sheet expansion ($\tau_n > 1$). The dotted line is the average over all (We, δ) for $\tau_n < 1$. Symbols in $We = 186$ (◯), 367 (▷), 700 (★), 1340 (□), 2435 (◇).

$$\begin{aligned}
\langle X\rangle^1 &: \text{average over sheet expansion,} && \tau_n < 1\\
\langle X\rangle^2 &: \text{average over sheet retraction,} && 1 < \tau_n < \tau_r\\
\langle X\rangle^3 &: \text{average after full sheet retraction from the edge,} && \tau_n > \tau_r\\
\langle X\rangle^{2\text{-}3} &: \text{average after sheet expansion,} && \tau_n > 1,\\
\langle X\rangle &: \text{average over all time} && \tau_n > 0.
\end{aligned} \tag{20}$$

As seen in Fig. 19a, the average speed during sheet expansion is very close to the theoretical speed of radially-ejected droplets, i.e., $\langle v/v_T\rangle^1 \sim 1$, for all We and δ, which is expected from the definition of v_T. The corresponding standard deviation is about seven times smaller than the average value, which confirms the good collapse of the data already seen for $\tau_n < 1$ in Fig. 18. Furthermore, the Probability Distribution Function $PDF\left(\langle v/v_T\rangle^1\right)$, that includes all droplets ejected for $\tau_n < 1$, follows a Gaussian distribution of mean 1.05 and standard deviation 0.2 (Fig. 19a - inset). During the retraction and collapse of the sheet (so as soon as $\tau_n \gtrsim 1$), both the average $\langle v/v_T\rangle^{2\text{-}3}$ and corresponding standard deviation decrease linearly with increasing δ (Fig. 19b). The larger scatter at small δ can be attributed to the presence of additional ejection mechanisms (namely the tangential droplets and the filament collapse). . There is almost no dependence to We, which indicates that the sheet asymmetry (measured by δ) pilots the droplet ejection pattern during the sheet retraction and collapse only.

C. Droplet mass

We now focus on the mass of the ejected droplets which is a key property that also determines the distance travelled. Information concerning mass estimation can be found in appendix A. The mass m of the ejected droplets is reported as a function of their normalized ejection time τ_n in Fig. 20a, for the six examples of Figs. 4 and 5. Contrary to the ejection speed v, the mass m varies on more than three orders of magnitude and it is scattered at all time. Nevertheless, viscosity sets a lower bound to the size of ejected droplets. In the context of partial coalescence, the inhibition of inertial liquid break-up by viscosity was observed for Ohnesorge numbers $Oh \gtrsim 0.025$ [76, 77]. It here corresponds to a minimum radius of 0.02 mm, and a mass $m/M_0 \simeq 5\times10^{-7}$. This size is slightly below the resolution of our camera. m is clearly bounded by a maximal mass that increases with time for $\tau_n < 1$ and saturates to a constant value for $\tau_n > 1$. This maximal droplet mass is still 50 times smaller than the mass $M_0 = 4\pi\rho R_0^3/3$ of the impacting drop.

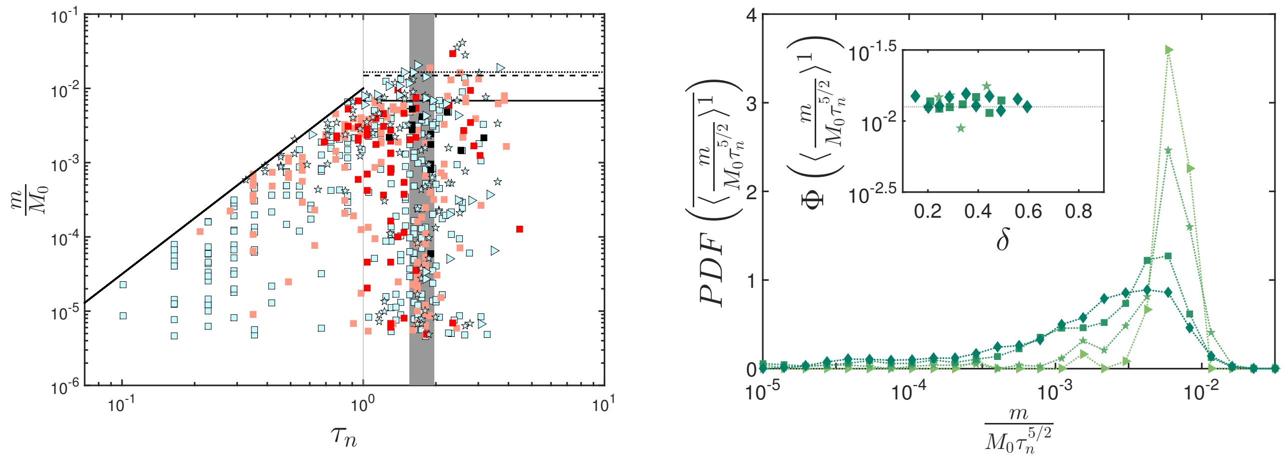

(a) (b)

FIG. 20. (Colour online) (a) Time evolution of the mass m of the ejected droplets (normalized by the mass M_0 of the impacting drop) as a function of their normalized time of ejection τ_n, for the six examples of Figs. 4 and 5. Each data point corresponds to a single droplet. Symbols correspond to Weber number, $We = 367$ (▷), 700 (★), 1340 (□), while colours indicate scenario, I (black), II (reddish/grey) and III (blue/clear). The grey area indicates the time τ_r at which the sheet has fully retracted from the edge (average across We and δ, plus/minus standard deviation). The inclined solid line represents Eq. (21). The horizontal lines correspond to the cut-off mass $\Phi(m/M_0)$ during retraction with $We = 367$ (dotted), $We = 700$ (dashed) and $We = 1340$ (solid). (b) Probability Distribution Function (PDF) of the normalized mass $m/(M_0{\tau_n}^{5/2})$ of droplets ejected during sheet expansion ($\tau_n < 1$), pooled per We (all δ together). The symbols correspond to different $We = 186$ (◯), 367 (▷), 700 (★), 1340 (□), 2435 (◇). Inset: Saturation value Φ of the PDF, for each We and δ. The dotted line corresponds to the coefficient of Eq. (21).

The increase of this upper bound on mass during sheet expansion ($\tau_n < 1$) satisfies a power law

$$\frac{m}{M_0} \leq 0.013\tau_n^{5/2}, \tag{21}$$

that is valid for each scenario so it is presumably independent of the offset δ. Equation (21) suggests to analyze the statistical distribution of droplet mass, normalized by $\tau_n^{5/2}$ (Fig. 20b). The Probability Distribution Function

$$PDF\left(\overline{\langle \frac{m}{M_0\tau_n^{5/2}} \rangle^1}\right)$$

is calculated on all our data, pooled per We (all δ together), which is denoted with a simple overline. This distribution presents a mode that approximately varies as $We^{-0.2}$, so faster incoming drops generate smaller ejected droplets. There is a cut-off on the right end of this PDF, which corresponds to the maximal mass. We define the maximal value of any variable X as the cut-off $\Phi(X)$ of its statistical distribution. This cut-off is here obtained by approximating the tail of the corresponding Cumulative Distribution Function (CDF) of X with a quadratic function that reaches a maximum of 1 in Φ. The least-square fit is performed with data from quantiles 0.85 to 0.995.

The cut-off mass at $\tau_n < 1$ is determined for each δ and We independently (Fig. 20b - inset). It is remarkably independent of δ and We, and its average value is given by Eq. (21). Similarly to the droplet speed, once this cut-off mass is expressed as a function of the sheet time τ_n, any explicit dependence to We and δ disappears, which is characteristic of the droplets radially ejected during sheet expansion.

During retraction and after sheet collapse, the distribution and cut-off value of the mass are almost independent of δ, and they slightly decrease with increasing We. A more detailed analysis is available in appendix C.

D. Distance travelled by the droplets

The ballistic trajectory $\mathbf{x}(t) = x(t)\mathbf{e}_x + z(t)\mathbf{e}_z$ of each ejected droplet in a vertical plane $(\mathbf{e}_x, \mathbf{e}_z)$ can be computed from Newton's law, as a function of its mass m and ejection speed v (Appendix B).

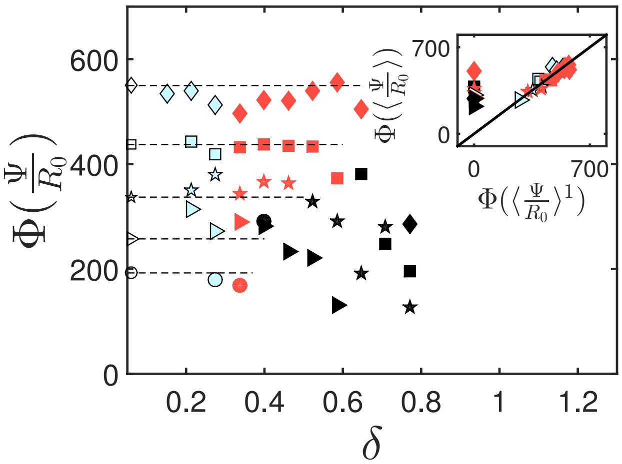

FIG. 21. (Colour online) Maximum horizontal distance $\Phi(\Psi/R_0)$ travelled by the ejected droplets, pooled together per We and δ. Symbols correspond to different We (table I) while colours indicate scenario, I (black), II (reddish/grey) and III (blue/clear). The dashed lines correspond to Eq. (22). Inset: $\Phi(\Psi/R_0)$ during the whole ejection process compared to the one dictated by the droplets ejected during the sheet extension. The solid line is the bisector. Symbols correspond to different $We = 186$ (◯), 367 (▷), 700 (★), 1340 (□), 2435 (◇).

We here consider the horizontal direction of ejection $\mathbf{e}_x$, and compute $x(t)$, the distance travelled horizontally since ejection, no matter in which direction θ_v. Owing to air drag, the horizontal speed decreases with time and $x(t)$ reaches an asymptotic value $\Psi = \lim_{t\to\infty} x$ called the aerodynamic wall [78].

The cut-off $\Phi(\Psi)$ of the statistical distribution of Ψ is calculated by pooling all ejected droplets from different experiments at given We and δ (Fig. 21). When the offset δ is in the range of scenarios (II) and (III), $\Phi(\Psi)$ is fairly independent of δ. By contrast, when δ is in the range of scenario (I), $\Phi(\Psi)$ decreases with increasing δ. The similarity of $\Phi(\langle\Psi\rangle)$ and $\Phi(\langle\Psi\rangle^1)$, illustrated in inset of Fig. 21, suggests that the cut-off distance $\Phi(\Psi)$ is already reached by the droplets ejected during the sheet expansion ($\tau_n < 1$), if any [i.e., for scenarios (II) and (III)]. Droplets ejected afterwards ($\tau_n > 1$) can travel as far, but not significantly farther. The upper bound of Ψ first increases with time, until a maximum value Ψ_M is reached slightly before $\tau_n = 1$. This maximum Ψ_M during expansion can be predicted from the maximal mass $\Phi\left(m/M_0\right)$ given by Eq. (21), and the quantile 90% of the ejection speed. During sheet expansion, the speed distribution is approximately gaussian with mean v_T and standard deviation $0.2v_T$ (Fig. 19), so this quantile is estimated as $Q_{90}\left(v_T/V_0\right) = \left(1 + 0.2\sqrt{2}\mathrm{erf}^{-1}(0.8)\right)\left(v_T/V_0\right) = 1.26 v_T/V_0$. Since both mass and speed bounds are independent of δ during sheet expansion (Figs. 19a - and 20b - inset), Ψ_M is also independent of δ. Droplets of scenario (I) are only ejected in $\tau_n > 1$, when the average speed is already low (Fig. 18 - middle) while the mass is not necessarily larger (see Appendix C). As a result, droplets from scenario (I) travel much less far than those of other scenarios.

For the range of We considered in this study, Ψ_M is approximately given by

$$\frac{\Psi_M}{R_0} \simeq 23\, We^{2/5}, \tag{22}$$

which provides a practical first-order approximation of the distance that ejected droplets can possibly reach at a given We in the worst case scenario (scenarios II and III).

This upper bound on travelled distance, originally derived from droplets ejected during sheet expansion, seems to hold for droplets ejected when the sheet retracts and collapses. This implies that the sheet early dynamics conditions the maximum distance travelled by the droplets for scenarios (II) and (III) independently on the offset.

E. Global effects of the sheet asymmetry

The previous section showed that the maximum distance travelled by the ejected droplets is fairly insensitive to the sheet asymmetry (i.e. to the offset). However, this asymmetry still greatly influences the dispersal ability. For example, the mass of droplets ejected at a given distance Ψ (usually during sheet retraction and collapse) can be 10 times larger than the mass of droplets ejected during the sheet expansion, provided that the offset is sufficiently small.

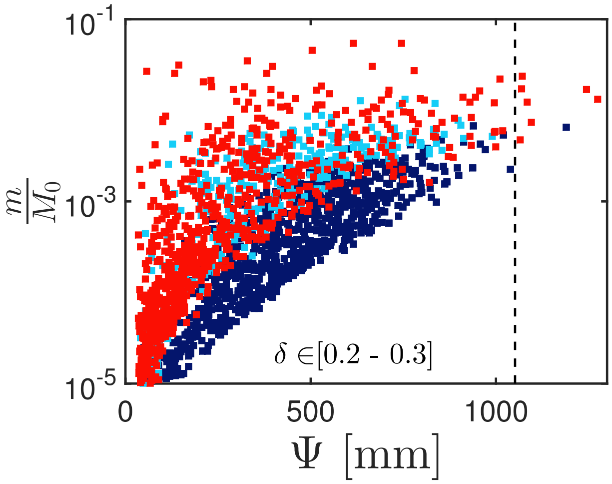

(a)

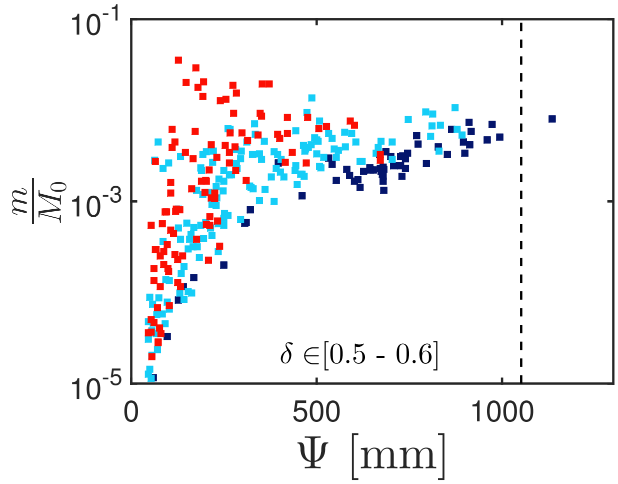

(b)

FIG. 22. (Colour online) Mass m of the ejected droplets, normalized by the mass of the impacting drop, as a function of their travelled distance Ψ for $We = 1340$ (□). (a) $\delta \in [0.2 - 0.3]$. (b) $\delta \in [0.5 - 0.6]$. The colour indicates the ejection time: during sheet expansion ($\tau_n < 1$, dark blue), during sheet retraction ($1 < \tau_n < \tau_r$, light blue) and after sheet collapse ($\tau_n > \tau_r$, red). The vertical dotted lines represent Eq. (22).

This is illustrated in the $(m/M_0, \Psi)$ diagrams of Figs. 22a and 22b for two different ranges of δ. . Tangentially-ejected droplets are often among these outperforming droplets, since they inherit from a mass similar to the radially-ejected droplets, with a possibly larger speed. Figure 22a also displays a large number of small droplets ejected during the collapse phase which correspond to the filament breakup mechanism.

In terms of number of droplets, the Cumulative Distribution Function (CDF) of the normalized time τ_n at which droplets are ejected, i.e., the number of droplets ejected before a given τ_n, is represented in Fig. 23a for the 6 examples of Figs. 4 and 5. The number of droplets increases with We and decreases with increasing δ. For all scenarios, the ejection rate (slope of the CDF) remains steady during sheet extension, then it strongly decreases during retraction. In scenarios (II) and (III), there is an additional outburst of droplets at the moment of collapse τ_r, which corresponds to the filament breakup mechanism. The ejection rate decreases again for larger τ_n. For scenarios (II) and (III), the first ejections occur during the expansion of the sheet. Conversely, in the isotropic scenario (I), ejections only start during the retraction of the sheet.

The average number N of ejected droplets per impact is represented in Fig. 23b, where data from all experiments have been again pooled by We and δ. This number of droplets increases with We, and it decreases almost quadratically with increasing offset δ, among others since the fraction of the impacting drop that crosses the edge decreases. The number of droplets vanishes in $\delta = 0.9$, which also corresponds to a vanishing liquid sheet [Eq. (8)]. As confirmed in Fig. 23b, it can be approximated by

$$N = 0.02\, We^{1.4} (0.9 - \delta)^2. \tag{23}$$

The increase of number of droplets with the decrease of δ could originate from three main causes: as δ decrease, (i) more fluid crosses the edge, (ii) the filament breakup mechanism occurs which is responsible for a high number of small droplets and (iii) the shedding of droplets begins earlier. The offset thus influences the number and mass of the droplets. The importance of these results in relation to pathogen dispersal is discussed in the following section.

VI. DISCUSSION

There are many different configurations in which raindrops can impact on plant leaves and subsequently fragment into droplets. Some of these configurations are particularly efficient at ejecting these droplets far away. They are consequently of primary relevance for the dispersal of pathogens initially present on infected leaves. A common feature observed in most impact configurations is the formation and break-up of an asymmetric liquid sheet, connected to the substrate on one side, and delimited by a rim entirely in the air on the other side. In this paper, we have investigated the impact of a drop at speed V_0 next to the straight edge of a flat horizontal substrate. A similar sheet is formed

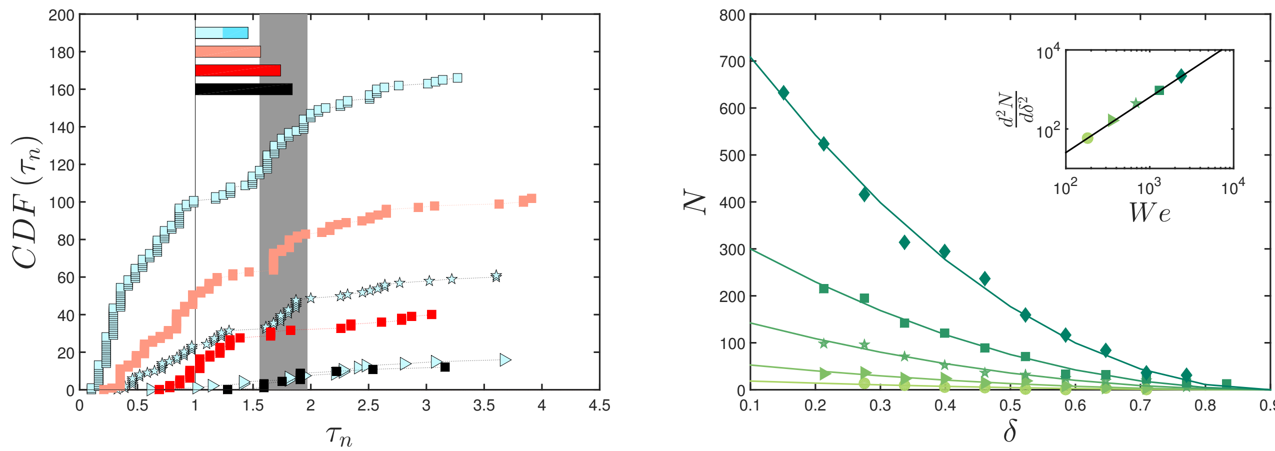

(a)

(b)

FIG. 23. (Colour online) (a) Non-normalized Cumulative Distribution Function (CDF, expressed in number of ejected droplets) of the normalized time τ_n for the six examples of Figs. 4 and 5. Symbols correspond to Weber number, $We = 367$ (▷), 700 (★), 1340 (□), while colours indicate scenario, I (black), II (reddish/grey) and III (blue/clear). The grey area indicates the time τ_r at which the sheet has fully retracted from the edge (average across We and δ, plus/minus standard deviation). (b) Average number N of droplets ejected per impact, as a function of δ. Symbols in $We = 186$ (◯), 367 (▷), 700 (★), 1340 (□), 2435 (◇). Solid lines are Eq. (23). (Inset) Second derivative of N with respect to δ, as a function of We. The solid line corresponds to $d^2N/d\delta^2 = 0.04\,We^{1.4}$ in Eq. (23).

and fragmented, but the kinematics is much easier to visualize and quantify since both the sheet and the ejected droplets move approximately in the plane of the substrate. Moreover, this configuration involves only two relevant dimensionless parameters: the offset from the edge d and the Weber number We. We have varied both parameters, with the latter in a range similar to that of raindrops. From video recordings, we have systematically tracked and quantified the motion of both the sheet and the ejected droplets.

The evolution of the sheet in the direction normal to the edge is approximately symmetric in time. It is advantageously described by measuring the time from its birth, at the instant t_d at which the liquid takes-off from the substrate. The duration of the sheet extension $t_{nM} - t_d$ is then approximately proportional to the capillary time t_c [Eq. (11)], with a corrective factor that mostly depends on the ratio δ between the offset d and the maximum spreading distance on the solid R_{sM}. The maximum extension l_{nM} of the sheet normal to the edge is approximately proportional to $V_0 t_c$ [Eq. (9)], with again a corrective factor to take the initial spreading on solid into account. This latter is linearly decreasing with δ. Remarkably, the corresponding acceleration normal to the edge, which then scales as V_0/t_c, is constant with time and does not depend on δ. We have also shown that, against intuition, the sheet can extend farther from the substrate when a drop impacts at a distance d from a flat edge than when it impacts at the centre of a pole of radius d.

The evolution of the sheet along the edge is however not symmetric in time. Its extension follows the adjacent spreading on the substrate, while its retraction involves dewetting of the edge. The important scatter of the corresponding data suggests the presence of uncontrolled contact line pinning during this retraction phase. The asymmetry of the sheet shape strongly depends on δ. We identified three different scenarios, that correspond to characteristic shapes of the sheet. The boundaries between these scenarios can be rationalized by considering the competition of sheet kinematics in directions normal and tangent to the edge.

We characterized ejected droplets statistically in terms of number, mass, speed, direction and time of ejection. The ejection statistics is time-dependent, and varies with δ and We. Nevertheless, most of the dependence on δ is accounted for when the rescaled ejection time τ_n (ejection time normalized by the time of maximal extension of the sheet) is used. This is especially true during sheet expansion, when droplets are mostly ejected radially starting from a time that increases with δ. Droplets ejected at the same normalized time have approximately the same speed, which decreases with this time. Their mass distribution is more scattered, but it is bounded by a maximal ejectable mass that is an increasing function of τ_n only.

When the sheet retracts and collapses, both droplet speed and mass distributions spread considerably (at least for the two most asymmetrical sheet scenarios) and do depend on δ. This is partly due to the additional ejection of tangentially-ejected droplets, i.e., droplets ejected in a direction parallel to the sheet and normal to its retraction. In the most asymmetrical cases (small δ), the final collapse of the sheet near to the edge triggers out-of-plane ejection of a large number of tiny droplets.

We estimate the maximum horizontal distance that each ejected droplet would travel ballistically, as a function of its mass and ejection speed. The upper bound of this distance is independent of δ for the two most asymmetric sheet scenarios. It can be predicted by considering the speed and maximum mass of droplets ejected during the sheet expansion only. Droplets ejected during the retraction and collapse of the sheet can go as far but not significantly farther. However, for the same travelled distance, their mass can be larger by a factor of 10. The decrease in offset allows these larger droplets to increase their distance travelled while staying bounded by the distance predicted by the sheet early dynamics.

These results can be discussed in the context of rain-induced dispersal of foliar pathogens. Each droplet ejected from an infected leaf is susceptible to carry some pathogenic content. The number, mass and ejection speed of these droplets are key inputs for the epidemiological models based on droplet ballistics [79]. The likelihood of infection is a combination of these factors. Our experiments at $We \in [180, 2500]$ covered most of the range of Weber number experienced by raindrops ($We \in [28, 5800]$). We may therefore expect that our conclusions on the impact near a straight edge are still valid, at least qualitatively, for more complex impact scenarios encountered by raindrops on leaves. In particular, the number, the speed of the ejected droplets and their maximal travelled distance all increase with increasing We, but at the same time the maximal droplet mass decreases. The asymmetry of the sheet, here measured with δ and omnipresent in complex natural impacts, does not seem to increase the maximum distance travelled by the droplets. But it does increase their number and maximal mass at a given distance. It should consequently increase the likelihood that a droplet containing a critical amount of pathogens lands on a distant leaf, and so increase the overall dispersal speed of the disease.

Current mitigation techniques of foliar diseases, such as the intensive use of chemicals or genetically modified organisms can be complemented by polyculture [13, 80, 81] or integrated culture [82]. The risk of epidemics is a major factor to take into account in the optimization of crops [81]. Our work has showed how both impact speed and distance from an edge shape the statistics of ejected droplets upon raindrop impact. Our results can help the development of agricultural epidemiological models.

ACKNOWLEDGMENTS

This work is supported by the FRIA/FNRS. The authors also thank the USDA-NIFA Specialty Crop Research Initiative Grant Award No. MDW-2016-04938, and MIT REED and Edgerton Funds. S.L is grateful for the support of the Rotary Foundation. The authors also thank L. Tadrist and Y. Wang for fruitful discussions.

Appendix A: Droplet tracking and mass calculation

On each frame, all the objects detached from the main body of the sheet were considered as ejected droplets. Their area, perimeter and position with respect to the impact point was recorded. Their trajectory was then reconstructed. During this process, only objects that could be consistently tracked over at least five frames were considered. This condition removed fluid particles that either quickly merged with others, or that quickly fragmented. The ejection time of the droplets is defined as the time at which they were first detected. The ejection velocity v is calculated from the first frames after ejection. Merging and fragmentation of droplets are common, especially during sheet retraction in the most asymmetrical scenarios (II - III). We chose to only consider as droplets the objects that either left the field of view before the end of the recording, or that were still present in its last frame. By doing so, we reduced the likelihood of counting multiple times the same fluid particle. However we also arbitrarily selected large merged droplets instead of keeping the smaller droplets that were initially ejected. Furthermore, sometimes the residues of the collapsed sheet did not fully fragment by the time they left the field of view.

Estimating the mass m of the ejected droplets is challenging. Indeed, they are highly deformed when they pinch off from the liquid sheet, and they need some additional time to relax to a quasi-spherical equilibrium shape resulting from a balance of aerodynamic drag and surface tension [57]. This relaxation time is of the order of r^2/ν, where r is such that $m/\rho = 4\pi r^3/3$. Moreover, droplet collisions are common, especially when the high asymmetry of the sheet leads to antagonist motions of the rim. It is therefore likely that the tracked droplets leave the field of view before they become spherical.

We here estimate the droplet volume $\Omega = m/\rho$ based on a combination of the perimeter P and the area A seen and measured on each image. A droplet pinching off from a fluid ligament is initially elongated, so at first order it can be approximated by a pill shape, i.e., a cylinder of length L and radius R surrounded by two spherical caps of radius R. When $L \gg R$, Ω, A and P are proportional to R^2L, RL and L, respectively, so the ratio $\Omega P/A^2$ should be constant.

In general (for any L and R),

$$\frac{\Omega P}{A^2} = \frac{2\pi x^2 + \left(2\pi^2 + \frac{8\pi}{3}\right) x + \frac{8\pi^2}{3}}{4x^2 + 4\pi x + \pi^2} \tag{A1}$$

where $x = L/R$. The ratio $\Omega P/A^2$ indeed tends to a constant value of $\pi/2$ for an elongated pill ($x \gg 1$). In the other limit of a quasi-spherical pill ($x \ll 1$), $\Omega P/A^2 \simeq 8/3$, which is slightly larger. More complicated elongated shapes, such as when the sheet collapses after separation from the edge (scenario III), could be seen as a sum of elongated droplets, and it is likely that their ratio $\Omega P/A^2$ remains in the range $[\pi/2, 8/3]$.

In order to estimate the droplet volume, we first calculate an approximation of x. Since $P = 2R(\pi + x)$ and $A = R^2(\pi + 2x)$, x satisfies the second order equation:

$$x^2 + 2\left(\pi - \frac{P^2}{4A}\right) x + \pi\left(\pi - \frac{P^2}{4A}\right) = 0 \tag{A2}$$

This equation admits a single positive solution x when $P^2 \geq 4\pi A$ (the equality yields a spherical droplet). The volume is then calculated from Eq. (A1).

In conventional image processing functions (e.g., in Matlab), A is calculated as the sum of the selected pixels, while P is calculated by joining the centres of the edge pixels. Consequently, A is overestimated compared to P, which may erroneously result in $P^2 < 4\pi A$. This artefact may be corrected by removing the excess of area, i.e., by replacing A by $A - \epsilon P/2$, where ϵ is the pixel size. This correction is sufficient to ensure $P^2 \geq 4\pi A$ for all droplets.

Appendix B: Travelled distance: the aerodynamic wall

The ballistic trajectory $\mathbf{x}(t) = x(t)\mathbf{e}_x + z(t)\mathbf{e}_z$ of each ejected droplet can be computed from Newton's law, as a function of its mass m and ejection speed v:

$$\begin{aligned} m\frac{d^2\mathbf{x}}{dt^2} &= -mg\mathbf{e}_z - 6\pi\mu_a r\frac{d\mathbf{x}}{dt}\left[1 + \frac{c}{100}Re^{2/3}\right] \text{ for } Re = \frac{2r\rho_a}{\mu_a}\left|\frac{d\mathbf{x}}{dt}\right| < 1000 \\ m\frac{d^2\mathbf{x}}{dt^2} &= -mg\mathbf{e}_z - \frac{3(1+c)}{125}\frac{\pi}{2}\rho_a r^2\frac{d\mathbf{x}}{dt}\left|\frac{d\mathbf{x}}{dt}\right| \text{ for } Re > 1000 \end{aligned} \tag{B1}$$

where Re is the Reynolds number, $r = (3m/4\pi\rho)^{1/3}$ is the droplet radius, c is a fitting parameter, and ρ_a and μ_a are the density and dynamic viscosity of the air, respectively. We here consider $\mathbf{e}_x$ as the horizontal direction of ejection, and $x(t)$ is the distance travelled horizontally since ejection, no matter in which direction θ_v. In Eq. (B1), the air drag is calculated with an approximation valid for spherical objects in a large range of Reynolds number (cf. similar models in [83]). A fit on experimental data from [84] yields $c \simeq 16$.

Owing to air drag, the horizontal speed decreases with time and $x(t)$ reaches an asymptotic value $\Psi = \lim_{t\to\infty} x$ called the aerodynamic wall [78].

First, Eq. (B1) is non-dimensionalized with characteristic timescale T and length scale L defined in the limit of small Reynolds number,$T = 2\rho r^2/(9\mu_a)$, $L = gT^2$, $\mathbf{y} = \mathbf{x}/L$, $\tau = t/T$

from which we obtain:

$$\begin{aligned} \frac{d^2\mathbf{y}}{d\tau^2} &= -\mathbf{e}_z - \left[1 + \frac{c}{100}\beta^{2/3}\left|\frac{d\mathbf{y}}{dt}\right|^{2/3}\right]\frac{d\mathbf{y}}{d\tau} \text{ if } \beta\left|\frac{d\mathbf{y}}{dt}\right| < 1000 \\ \frac{d^2\mathbf{y}}{d\tau^2} &= -\mathbf{e}_z - \frac{1+c}{1000}\beta\left|\frac{d\mathbf{y}}{dt}\right|\frac{d\mathbf{y}}{d\tau} \text{ if } \beta\left|\frac{d\mathbf{y}}{dt}\right| > 1000 \end{aligned} \tag{B2}$$

where the dimensionless parameter β is defined as $\beta = (mg\rho_a)/(3\pi\mu_a^2) = (4\rho_a\rho g r^3)/(9\mu_a^2)$.

This differential equation can be integrated, with an initial horizontal dimensionless speed $d\mathbf{y}/d\tau|_{\tau=0} \cdot \mathbf{e}_x = u = (9\mu_a)/(2\rho g r^2)v$.

1. Exact solution at low Reynolds number

There is an exact solution to Eq. (B2) at low Reynolds number, i.e., for droplets that are sufficiently small so $\beta \ll 1$. Equation B2 then simplifies into:

$$\frac{d^2\mathbf{y}}{d\tau^2} + \frac{d\mathbf{y}}{d\tau} = -\mathbf{e}_z \tag{B3}$$

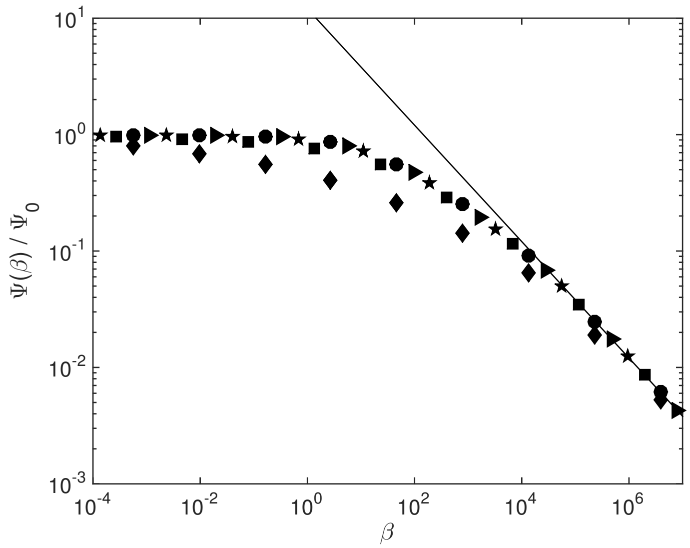

FIG. 24. Maximum travelled horizontal distance Ψ, as a function of the dimensionless droplet size β. Each symbol corresponds to a different ejection speed v: ($\bigcirc$) $v = 10^{-3}$ m/s, ($\triangleright$) $v = 10^{-2}$ m/s, ($\bigstar$) $v = 10^{-1}$ m/s, ($\square$) $v = 1$ m/s, ($\diamondsuit$) $v = 10$ m/s. The solid line corresponds to $\Psi(\beta)/\Psi(0) \simeq 12\beta^{-1/2}$.

Time-integration yields $\mathbf{y} = (1 - e^{-\tau})\,(u\mathbf{e}_x + \mathbf{e}_z) - \tau\mathbf{e}_z$.

The maximum horizontal distance travelled is then $y_\infty = \lim_{\tau\to\infty} \mathbf{y}\cdot\mathbf{e}_x = u$ or, in dimensional form $\Psi_0 = \Psi(\beta \ll 1) = y_\infty L = 2\rho r^2 v/(9\mu_a)$.

The condition $Re < 1$ yields

$$\frac{2r\rho_a L}{\mu_a T} < 1 \Rightarrow \beta < 1 \tag{B4}$$

2. Numerical solution for any Reynolds number

The droplets ejected during the sheet fragmentation are in the range $m/M_0 \in [3\times10^{-6}, 3\times10^{-2}]$ (Fig. 20a), which corresponds to $r \in [0.035, 0.75]$ mm and $\beta \in [0.67, 6700]$. The ejection speed can reach 10 m/s, so the Reynolds number at ejection can be as high as 1000. Therefore we need to solve Eq. (B2) numerically.

The solution is represented for dimensionless size $\beta \in [10^{-4}, 10^7]$ and ejection speed $v \in [10^{-3}, 10]$ m/s, in Fig. 24. Once normalized by Ψ_0, the aerodynamic wall Ψ does not depend on ejection speed v anymore, except for very large speed (here $v = 10$ m/s) where Ψ/Ψ_0 can be twice smaller than at moderate speed. So in first approximation,

$$\frac{\Psi}{\Psi_0} = F(\beta) \tag{B5}$$

where $F(\beta) \to 1$ for $\beta \to 0$ and $F(\beta) \to 12/\sqrt{\beta}$ when $\beta \to \infty$.

The function $F(\beta)$ satisfies $F(0) = 1$ (low Reynolds limit), and it scales as $F \sim \beta^{-1/2}$ for $\beta \gg 1$ (high Reynolds limit). Since β is only dependent on droplet size r and not on speed v, the aerodynamic wall at a distance Ψ is always approximately proportional to the ejection speed v.

Appendix C: Droplets masses after maximum extension

During retraction, the mass distribution is almost independent of δ, and it is slightly shifted to lower mass with increasing We. By contrast, the distribution after collapse does depend on both δ and We. The cut-off Φ of the mass distribution of ejected droplets is again calculated separately for each We and δ, first during sheet retraction (Fig. 25a) and second after sheet collapse (Fig. 25b). During retraction, the variation of $\Phi\left(\langle m/M_0\rangle^2\right)$ with δ is very small. Consequently, data from different δ can be pooled, which reveals a power-law dependence in We (Fig. 25a -

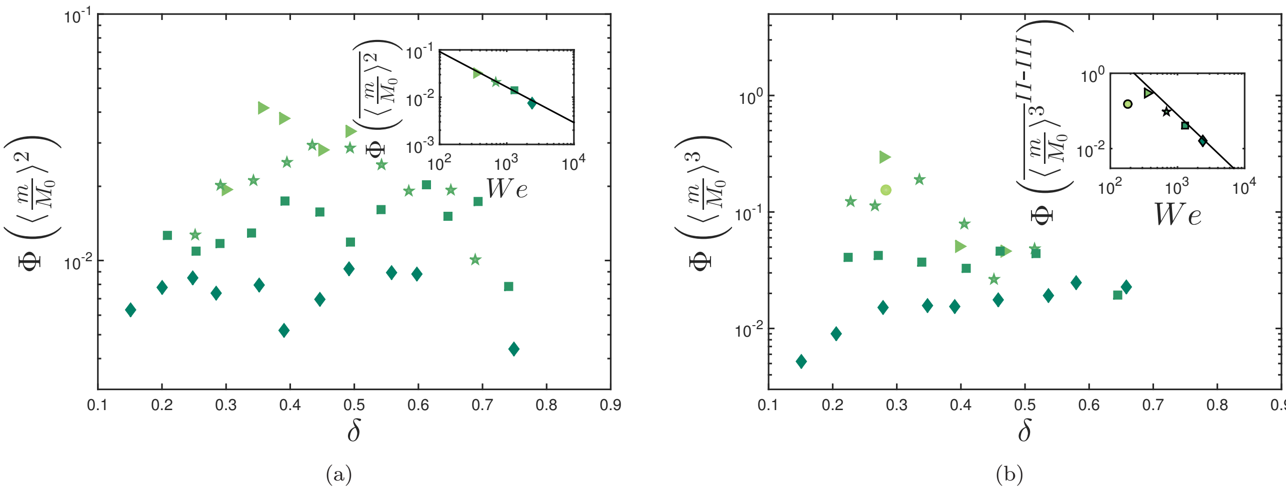

FIG. 25. (Colour online) Cut-off Φ of the mass distribution of ejected droplets, pooled per We and δ: (a) during the retraction of the sheet, and (b) after collapse of the sheet. Symbols correspond to different $We = 186$ ($\bigcirc$), 367 ($\triangleright$), 700 ($\bigstar$), 1340 ($\square$), 2435 ($\diamond$). Insets: Dependence to We of the cut-off Φ: (a) after pooling all δ. The solid line is Eq. (C1). (b) After pooling scenarios (II) and (III). The solid line is Eq. (C2).

inset) given by

$$\Phi\left(\overline{\langle\frac{m}{M_0}\rangle^2}\right) \simeq 2.9\,We^{-3/4}. \tag{C1}$$

After the collapse of the sheet, $\Phi\left(\langle m/M_0\rangle^3\right)$ is almost independent of δ at high We, but it sharply decreases with increasing δ at lower We. The pooling of scenarios (II) and (III) reveals a decrease of the average cut-off with increasing We given by

$$\Phi\left(\overline{\langle\frac{m}{M_0}\rangle^3}^{II\text{-}III}\right) \simeq 10^4\,We^{-1.7} \tag{C2}$$

The comparison of Eq. (C1) and Eq. (C2) reveals that, for $We \lesssim 4000$, the mass cut-off is larger after collapse than during retraction of the sheet. This fact could be the consequence of (i) the likely merging of ejected droplets after collapse, and (ii) the presence of a very large liquid filament detached from the edge [e.g., in scenario (III)] that does not instantly destabilize into smaller droplets.

[1] E.-C. Oerke, "Crop losses to pests," Journal of Agricultural Science **144**, 31–43 (2006).

[2] I. B. Pangga, J. Hanan, and S. Chakraborty, "Pathogen dynamics in a crop canopy and their evolution under changing climate," Plant Pathology **60**, 70–81 (2011).

[3] H. Fones and S. Gurr, "The impact of septoria tritici blotch disease on wheat: An eu perspective," Fungal Genetics and Biology **79**, 3–7 (2015).

[4] R. D. Magarey, T. B. Sutton, and C. L. Thayer, "A simple generic infection model for foliar fungal plant pathogens," Phytopathology **95**, 92–100 (2005).

[5] A. Dalla Marta, R. D. Magarey, and S. Orlandini, "Modelling leaf wetness duration and downy mildew simulation on grapevine in italy," Agricultural and Forest Meteorology **132**, 84–95 (2005).

[6] A. Calonnec, J.-B. Burie, M. Langlais, S. Guyader, S. Saint-Jean, I. Sache, and B. Tivoli, "Impacts of plant growth and architecture on pathogen processes and their consequences for epidemic behaviour," European Journal of Plant Pathology **135**, 479–497 (2013).

[7] G. Garin, C. Fournier, B. Andrieu, V. Houlès, C. Robert, and C. Pradal, "A modelling framework to simulate foliar fungal epidemics using functional-structural plant models," Annals of Botany **114**, 795–812 (2014).

[8] B. D. L. Fitt, H. A. McCartney, and P. J. Walklate, "The role of rain in dispersal of pathogen inoculum," Annual review of phytopathology. **27**, 241–270 (1989).

[9] P. A. Paul, S. M. El-Allaf, P. E. Lipps, and L. V. Madden, “Rain splash dispersal of gibberella zeae within wheat canopies in ohio,” Phytopathology **94**, 1342–1349 (2004).
[10] G. N. Agrios, *Plant pathology* (London, 2005).
[11] P. J. Walklate, H. A. McCartney, and B. D. L. Fitt, “Vertical dispersal of plant pathogens by splashing. part ii: experimental study of the relationship between raindrop size and the maximum splash height,” Plant Pathology **38**, 64–70 (1989).
[12] X. Yang, L. V. Madden, L. L. Wilson, and M. A. Ellis, “Effects of surface topography and rain intensity on splash dispersal of colletotrichum acutatum,” Phytopathology **80**, 1115–1120 (1990).
[13] C. Gigot, S. Saint-Jean, L. Huber, C. Maumené, M. Leconte, B. Kerhornou, and C. de Vallavieille-Pope, “Protective effects of a wheat cultivar mixture against splash-dispersed septoria tritici blotch epidemics,” Plant Pathology **62**, 1011–1019 (2013).
[14] K. M. Reynolds, M. A. Bulger, L. V. Madden, and M. A. Ellis, “New methods using simulated rain to study the splash dispersal of plant pathogens,” Phytopathology (USA) **77**, 921–926 (1987).
[15] X. Yang, L. V. Madden, D. L. Reichard, R.D. Fox, and M. A. Ellis, “Motion analysis of drop impaction on a strawberry surface,” Agricultural and Forest Meteorology **56**, 67–92 (1991).
[16] I. Sache, “Short-distance dispersal of wheat rust spores by wind and rain,” Agronomie **20**, 757–767 (2000).
[17] S. Pietravalle, F. Van Den Bosch, S. J. Welham, S. R. Parker, and D. J. Lovell, “Modelling of rain splash trajectories and prediction of rain splash height,” Agricultural and Forest Meteorology **109**, 171–185 (2001).
[18] T. Gilet and L. Bourouiba, “Rain-induced ejection of pathogens from leaves: Revisiting the hypothesis of splash-on-film using high-speed visualization,” Integrative and Comparative Biology **54**, 974–984 (2014).
[19] T. Gilet and L. Bourouiba, “Fluid fragmentation shapes rain-induced foliar disease transmission,” Journal of the Royal Society Interface **12**, 20141092 (2015).
[20] A. L. Yarin, “Drop impact dynamics: Splashing, spreading, receding, bouncing.” Annual Review of Fluid Mechanics **38**, 159–192 (2006).
[21] M. Marengo, C. Antonini, I. V. Roisman, and C. Tropea, “Drop collisions with simple and complex surfaces,” Current Opinion in Colloid and Interface Science **16**, 292–302 (2011).
[22] C. Josserand and S. T. Thoroddsen, “Drop impact on a solid surface,” Annual Review of Fluid Mechanics **48**, 365–391 (2016).
[23] A.-B. Wang and C.-C. Chen, “Splashing impact of a single drop onto very thin liquid films,” Physics of Fluids **12**, 2155–2158 (2000).
[24] C. Josserand and S. Zaleski, “Droplet splashing on a thin liquid film,” Physics of Fluids **15**, 1650–1657 (2003).
[25] R. Rioboo, C. Bauthier, J. Conti, M. Voué, and J. De Coninck, “Experimental investigation of splash and crown formation during single drop impact on wetted surfaces,” Experiments in Fluids **35**, 648–652 (2003).
[26] M. Rein, “Phenomena of liquid drop impact on solid and liquid surfaces,” Fluid Dynamics Research **12**, 61–93 (1993).
[27] B. Ray, G. Biswas, and A. Sharma, “Regimes during liquid drop impact on a liquid pool,” Journal of Fluid Mechanics **768**, 492–523 (2015).
[28] R. Rioboo, C. Tropea, and M. Marengo, “Outcomes from a drop impact on solid surfaces,” Atomization and Sprays **11**, 155–165 (2001).
[29] M. Reyssat, A. Pépin, F. Marty, Y. Chen, and D. Quéré, “Bouncing transitions on microtextured materials,” Europhysics Letters **74**, 306–312 (2006).
[30] C. Antonini, A. Amirfazli, and M. Marengo, “Drop impact and wettability: From hydrophilic to superhydrophobic surfaces,” Physics of Fluids **24**, 102104 (2012).
[31] P. K. Unnikrishnan, V. Vaikuntanathan, and D. Sivakumar, “Impact dynamics of high weber number drops on chemically modified metallic surfaces,” Colloids and Surfaces A: Physicochemical and Engineering Aspects **459**, 109–119 (2014).
[32] D. Khojasteh, M. Kazerooni, S. Salarian, and R. Kamali, “Droplet impact on superhydrophobic surfaces: A review of recent developments,” Journal of Industrial and Engineering Chemistry **42**, 1–14 (2016).
[33] Z. Levin and P. V. Hobbs, “Splashing of water drops on solid and wetted surfaces, hydrodynamics and charge separation,” Phil Trans Roy Soc London Ser A. Math Phys Sci **269**, 555–585 (1971).
[34] S. Mandre, M. Mani, and M. P. Brenner, “Precursors to splashing of liquid droplets on a solid surface,” Physical Review Letters **102**, 134502 (2009).
[35] J. Palacios, J. Hernández, P. Gómez, C. Zanzi, and J. López, “Experimental study of splashing patterns and the splashing/deposition threshold in drop impacts onto dry smooth solid surfaces,” Experimental Thermal and Fluid Science **44**, 571–582 (2013).
[36] G. Riboux and J. M. Gordillo, “Experiments of drops impacting a smooth solid surface: A model of the critical impact speed for drop splashing,” Physical Review Letters **113**, 024507–1–5 (2014).
[37] G. Riboux and J. M. Gordillo, “The diameters and velocities of the droplets ejected after splashing,” Journal of Fluid Mechanics **772**, 630–648 (2015).
[38] A. Rozhkov, B. Prunet-Foch, and M. Vignes-Adler, “Impact of water drops on small targets,” Physics of Fluids **14**, 3485–3501 (2002).
[39] E. Villermaux and B. Bossa, “Drop fragmentation on impact,” Journal of Fluid Mechanics **668**, 412– 435 (2011).
[40] C. Vernay, L. Ramos, and C. Ligoure, “Free radially expanding liquid sheet in air: Time-and space-resolved measurement of the thickness field,” Journal of Fluid Mechanics **764**, 428–444 (2015).
[41] S. Arora, C. Ligoure, and L. Ramos, “Interplay between viscosity and elasticity in freely expanding liquid sheets,” Physical Review Fluids **1**, 083302 (2016).

[42] Y. Wang and L. Bourouiba, "Drop impact on small surfaces: Thickness and velocity profiles of the expanding sheet in the air," Journal of Fluid Mechanics **814**, 510–534 (2017).
[43] I. V. Roisman, "Dynamics of inertia dominated binary drop collisions," Physics of Fluids **16**, 3438–3449 (2004).
[44] I. V. Roisman, C. Planchette, E. Lorenceau, and G. Brenn, "Binary collisions of drops of immiscible liquids," Journal of Fluid Mechanics **690**, 512–535 (2012).
[45] M. Reyssat, F. Pardo, and D. Quéré, "Drops onto gradients of texture," EPL **87**, 36003 (2009).
[46] B. A. Malouin Jr., N. A. Koratkar, A. H. Hirsa, and Z. Wang, "Directed rebounding of droplets by microscale surface roughness gradients," Applied Physics Letters **96**, 234103 (2010).
[47] V. Vaikuntanathan, R. Kannan, and D. Sivakumar, "Impact of water drops onto the junction of a hydrophobic texture and a hydrophilic smooth surface," Colloids and Surfaces A: Physicochemical and Engineering Aspects **369**, 65–74 (2010).
[48] J. C. Bird, R. Dhiman, H.-M. Kwon, and K. K. Varanasi, "Reducing the contact time of a bouncing drop," Nature **503**, 385–388 (2013).
[49] D. H. Kwon, H. K. Huh, and S. J. Lee, "Wettability and impact dynamics of water droplets on rice (oryza sativa l.) leaves," Experiments in Fluids **55**, 1691 (2014).
[50] R. Zhang, P. Hao, and F. He, "Drop impact on oblique superhydrophobic surfaces with two-tier roughness," Langmuir **33**, 3556–3567 (2017).
[51] J. C. Bird, S. H. Tsai, and H. A. Stone, "Inclined to splash: Triggering and inhibiting a splash with tangential velocity," New Journal of Physics **11**, 063017 (2009).
[52] Y. H. Yeong, J. Burton, E. Loth, and I. S. Bayer, "Drop impact and rebound dynamics on an inclined superhydrophobic surface," Langmuir **30**, 12027–12038 (2014).
[53] H. Fujimoto, S. Yoshimoto, K. Takahashi, T. Hama, and H. Takuda, "Deformation behavior of two droplets successively impinging obliquely on hot solid surface," Experimental Thermal and Fluid Science **81**, 136–146 (2017).
[54] G. Juarez, T. Gastopoulos, Y. Zhang, M. L. Siegel, and P. E. Arratia, "Splash control of drop impacts with geometric targets," Physical Review E - Statistical, Nonlinear, and Soft Matter Physics **85**, 026319 (2012).
[55] Y. Liu, M. Andrew, J. Li, J. M. Yeomans, and Z. Wang, "Symmetry breaking in drop bouncing on curved surfaces," Nature Communications **6**, 10034 (2015).
[56] N. Bremond and E. Villermaux, "Atomization by jet impact," Journal of Fluid Mechanics **549**, 273–306 (2006).
[57] É. Reyssat, F. Chevy, A.-L. Biance, L. Petitjean, and D. Quéré, "Shape and instability of free-falling liquid globules," EPL **80**, 34005 (2007).
[58] E. Villermaux and B. Bossa, "Single-drop fragmentation determines size distribution of raindrops," Nature Physics **5**, 697–702 (2009).
[59] I. V. Roisman, C. M. Weickgenannt, A. N. Lembach, and C. Tropea, "Drop impact close to a pore: experimental and numerical investigations," in *Proceedings of the 23rd Annual Conference on Liquid Atomization and Spray Systems, ILASS-Europe* (2010).
[60] C. Duez, C. Ybert, C. Clanet, and L. Bocquet, "Wetting controls separation of inertial flows from solid surfaces," Physical Review Letters **104**, 084503 (2010).
[61] "Supplementary material SM1_Fig4_We1300_scenarioI,".
[62] "Supplementary material SM2_Fig4_We1300_scenarioIIa,".
[63] "Supplementary material SM3_Fig4_We1300_scenarioIIb,".
[64] "Supplementary material SM4_Fig4Fig5_We1300_scenarioIII,".
[65] "Supplementary material SM5_Fig5_We350_scenarioIII,".
[66] "Supplementary material SM6_Fig5_We680_scenarioIII,".
[67] R. Rioboo, M. Marengo, and C. Tropea, "Time evolution of liquid drop impact onto solid, dry surfaces," Experiments in Fluids **33**, 112–124 (2002).
[68] A. L. Yarin and D. A. Weiss, "Impact of drops on solid surfaces: Self-similar capillary waves, and splashing as a new type of kinematic discontinuity," Journal of Fluid Mechanics **283**, 141–173 (1995).
[69] I. V. Roisman, R. Rioboo, and C. Tropea, "Normal impact of a liquid drop on a dry surface: Model for spreading and receding," Proceedings of the Royal Society A: Mathematical, Physical and Engineering Sciences **458**, 1411–1430 (2002).
[70] J. Eggers, M. A. Fontelos, C. Josserand, and S. Zaleski, "Drop dynamics after impact on a solid wall: Theory and simulations," Physics of Fluids **22**, 062101 (2010).
[71] H. Lastakowski, F. Boyer, A.-L. Biance, C. Pirat, and C. Ybert, "Bridging local to global dynamics of drop impact onto solid substrates," Journal of Fluid Mechanics **747**, 103–118 (2014).
[72] N. Laan, K. G. de Bruin, D. Bartolo, C. Josserand, and D. Bonn, "Maximum diameter of impacting liquid droplets," Physical Review Applied **2**, 044018 (2014).
[73] G. Lagubeau, M. A. Fontelos, C. Josserand, A. Maurel, V. Pagneux, and P. Petitjeans, "Spreading dynamics of drop impacts," Journal of Fluid Mechanics **713**, 50–60 (2012).
[74] A.-L. Biance, F. Chevy, C. Clanet, G. Lagubeau, and D. Quéré, "On the elasticity of an inertial liquid shock," Journal of Fluid Mechanics **554**, 47–66 (2006).
[75] M. Andrew, J. M. Yeomans, and D. O. Pushkin, "A solvable model of axisymmetric and non-axisymmetric droplet bouncing," Soft Matter **13**, 985–994 (2017).
[76] F. Blanchette and T. P. Bigioni, "Partial coalescence of drops at liquid interfaces," Nature Physics **2**, 254–257 (2006).
[77] T. Gilet, K. Mulleners, J. P. Lecomte, N. Vandewalle, and S. Dorbolo, "Critical parameters for the partial coalescence of a droplet," Physical Review E - Statistical, Nonlinear, and Soft Matter Physics **75**, 036303 (2007).

[78] C. Cohen, B. Darbois-Texier, G. Dupeux, E. Brunel, D. Quéré, and C. Clanet, "The aerodynamic wall," Proceedings of the Royal Society A: Mathematical, Physical and Engineering Sciences **470**, 1–20 (2013).

[79] S. Saint-Jean, M. Chelle, and L. Huber, "Modelling water transfer by rain-splash in a 3d canopy using monte carlo integration," Agricultural and Forest Meteorology **121**, 183–196 (2004).

[80] M. S. Wolfe, "Crop strength through diversity," Nature **406**, 681–682 (2000).

[81] T. Vidal, A.-L. Boixel, B. Durand, C. de Vallavieille-Pope, L. Huber, and S. Saint-Jean, "Reduction of fungal disease spread in cultivar mixtures: Impact of canopy architecture on rain-splash dispersal and on crop microclimate," Agricultural and Forest Meteorology **246**, 154–161 (2017).

[82] A. C. Newton, C. Gravouil, and J. M. Fountaine, "Managing the ecology of foliar pathogens: Ecological tolerance in crops," Annals of Applied Biology **157**, 343–359 (2010).

[83] R. Clift, J. R. Grace, and M. Weber, *Bubbles, drops, and particles* (Academic Press, London, 1978).

[84] Z. Duan, B. He, and Y. Duan, "Sphere drag and heat transfer," Scientific reports **5**, 12304 (2015).